

A μ SR Study of Current-Induced Destruction of Order in 1% Ti Doped Ca_2RuO_4

A μ SR STUDY OF CURRENT-INDUCED DESTRUCTION OF ORDER
IN 1% TI DOPED CA_2RUO_4

By Matthew NUGENT,

*A Thesis Submitted to the School of Graduate Studies in the Partial Fulfillment
of the Requirements for the Degree Master's of Physics and Astronomy*

McMaster University © Copyright by Matthew NUGENT August 24, 2021

McMaster University

Master's of Physics and Astronomy (2021)

Hamilton, Ontario (Department of Physics)

TITLE: A μ SR Study of Current-Induced Destruction of Order in 1% Ti Doped Ca_2RuO_4

AUTHOR: Matthew NUGENT (McMaster University)

SUPERVISOR: Dr. Graeme LUKE

NUMBER OF PAGES: xi, 71

Abstract

Due to its electrically activated phase transition from an insulator to a metal, Mott insulator Ca_2RuO_4 is a material with great potential in researching phase transitions and application of bolometric devices. Although pure Ca_2RuO_4 is very unstable and thus difficult to obtain in bulk, single-crystal form, a 1% doping of Ti for Ru stabilizes the material with minimal influence on its magnetic and electrical properties. This thesis uses μSR techniques to look at a single crystal of 1% Ti doped Ca_2RuO_4 under current in order to investigate the magnetic ordering of the material in its metallic state. From this we determine that Ca_2RuO_4 undergoes a destruction of long-range order when under sufficient current to induce its metallic state if one assumes adequate cooling power of the cryostat. In order to confirm the cooling power of the cryostat used, analyses on the Joule heating from the sample was performed, yielding mixed results, causing the question of whether this data was collected below the currentless ordering temperature of Ca_2RuO_4 to go unanswered.

Acknowledgements

I would like to take the time to thank all of those who have helped me on the road to the completion of this work. I would like to thank my supervisor, Dr. Graeme Luke, who has always been a guiding light for the direction of the research when a hurdle had to be overcome. Saying that I could not have done this without you would be an understatement and I appreciate the work you have done for me, my research, and the lab as a whole.

I would also like to thank my peers in Dr. Luke's group, as well as those in Dr. Gaulin and Dr. Imai's groups, as the collaborative atmosphere among us was always uplifting and gave an immediate place to ask a question. In particular, I would like to thank Megan Rutherford, Sudarshan Sharma, Zachary Cronkwright, and especially James Beare for being office mates that I could go to anytime to ask a question or discuss a problem. I would also like to thank Casey Marjerisson for all of her work in keeping the crystal growth lab organized and managing all of its operations. Your friendships made this possible.

I would also like to thank the instrument scientists and researchers at TRIUMF, particularly Sarah Dunsiger, Bassam Hitti, Gerald Morris, and Donald Asreanu as their many troubleshooting efforts are what allowed data collection to even occur through a rough start to the experiment.

Lastly, I would like to thank my parents Joe and Sue, as well as my wife Sunny for their constant support and words of encouragement throughout last 3 years. You mean the world to me. Thank you all so much!

Contents

Abstract	iii
Acknowledgements	iv
Declaration of Authorship	xi
1 Introduction	1
1.1 Ca_2RuO_4 the Mott Insulator	1
1.2 Material Context through Sr_2RuO_4	2
1.2.1 Conventional vs. Unconventional Superconductivity	3
1.2.2 Evidence for Sr_2RuO_4 as a p-Wave Superconductor	4
2 Background	5
2.1 Understanding Solid State Physics Models	5
2.1.1 Drude Model	5
2.1.2 Sommerfeld Model	7
2.1.3 Hartree-Fock Theory	10
2.2 Mott Insulators	12
2.2.1 Hubbard Bands	13
2.2.2 Antiferromagnetic Ordering	14
3 Ca_2RuO_4 Research	17
3.1 Ca_2RuO_4 phases	17

3.2	Research on Ca_2RuO_4 Magnetic and Transport Properties	21
3.2.1	Magnetization Data	21
3.2.2	Resistivity Data	22
3.3	Mott Insulator Transition	23
3.4	Current-Induced Magnetic Properties of Ca_2RuO_4	26
3.5	Spin-Orbit Coupling in Ca_2RuO_4	27
3.6	Titanium dopings in Ca_2RuO_4	28
4	μSR Techniques	31
4.1	Muon Creation and Decay	31
4.2	Asymmetry Plots	33
5	Synthesis of Ca_2RuO_4	37
5.1	Limitations of Crystal Growths and Experimentation	37
5.2	Synthesis Attempts	38
6	μSR Experiment at TRIUMF	41
6.1	μSR and study goals	41
6.2	μSR testing setup	42
6.2.1	The Sample Holder	42
6.2.2	Optimizing Signal to Noise	43
6.3	μSR Results	45
6.3.1	Zero-Current Measurements	45
6.3.2	Applied Current Measurements	46
6.4	Temperature control and Joule heating	49
6.4.1	Convective Heat Transfer Calculations	53
6.4.2	Resistivity Anomalies	56
6.4.3	Carbon Resistor Measurements	58
6.5	Summary	65

7	Conclusions	66
7.1	Research Summary	66
7.2	Further Research	67
7.3	Conclusion	68
	Bibliography	69

List of Figures

2.1	Free Electron Energy Curves	9
2.2	Hubbard Bands	14
2.3	Ground and Excited state in MI	16
3.1	S and L phases of Ca ₂ RuO ₄	18
3.2	Temperature-based Mott Transition	19
3.3	Pressure-based Mott Transition	20
3.4	Magnetization Temperature Sweep Data	22
3.5	Resistivity Temperature Sweep Data	23
3.6	Resistivity Temperature Sweeps Under Current	24
3.7	Resisitvity of Ca ₂ RuO ₄ at Variable Ti Doping	30
4.1	Pion Decay	32
4.2	Muon Decay Preference	34
4.3	μSR setup	35
5.1	Ca ₂ RuO ₄ Growth Attempts	40
6.1	Previous Pure Sample Data	42
6.2	Beamline setup	44
6.3	0mA Temperature Waterfall	47
6.4	0mA Current Comparison	48
6.5	30mA Temperature Waterfall	50

6.6	100mA Temperature Waterfall	51
6.7	Power Temperature Sweeps	53
6.8	Resistivities	57
6.9	30mA Resistance Test	59
6.10	100mA Resistance Test	60
6.11	Carbon Calibration	62
6.12	Carbon Power Sweeps	63
6.13	Carbon Corrections	64

List of Tables

6.1	Table of Current Densities and Lowest Temperatures Achieved	49
6.2	Table of Estimated Sample Temperatures from Thermometer Temperatures	56

Declaration of Authorship

The work presented in Chapter 5 and 6 were collaborative efforts. Synthesis of the materials at McMaster University were performed by myself as well as Graham Johnstone, Casey Marjerrison, and James Beare. The synthesis of the materials used in the experiment at TRIUMF were performed by Dr. Braden's group at the University of Cologne.

The μ SR experiments on 1% Ti doped Ca_2RuO_4 were performed using the M20 beamline located at TRIUMF in Vancouver, Canada. This experiment was performed by myself, James Beare, Megan Rutherford, and Sudarshan Sharma from McMaster University, Qi Sheng from Columbia University, and the instrument scientists Gerald Morris, Bassam Hitti, Donald Arseneau and Sarah Dunsiger.

Chapter 1

Introduction

1.1 Ca_2RuO_4 the Mott Insulator

The world of solid state physics research is dominated in recent times by exotic quantum mechanical phenomena. In particular, phenomena such as unconventional and high temperature cuprate superconductivity have been an incredibly popular field of study. Mott insulators are one researchable phenomenon outside of these areas, but is still a relevant topic of research for quantum phenomena. A Mott insulator is a material that should by logic of simple band theory be metallic and conducting, but is instead non-metallic and insulating. Ca_2RuO_4 is one such Mott insulator, and its close relation to the famous p-wave superconductor Sr_2RuO_4 gives it reason to be looked at with a similar degree of interest.

Mott insulators such as Ca_2RuO_4 as well as many exotic superconductors are strongly correlated materials. That is to say, the repulsive Coulomb interaction between electrons in the lattice heavily impacts the magnetic and electrical nature of the material. Understanding these interactions asks us to go beyond the simpler models for understanding solid state physics, such as the Drude and Sommerfeld models, and tuning the parameters of the materials tends to have surprising effects. Transitions to different quantum

phases tend to be relatively simple, and most of the resultant phases are worth studying to further understand the physics behind the lattice. Frequently, several quantum phases compete in these systems for prominence, becoming the dominant feature when the conditions are right. Of particular interest are materials with competing phases at or close to zero temperature, called quantum phase transitions. Quantum phase transitions are created through changes in factors such as pressure, current application, or charge doping.

Notably, Ca_2RuO_4 is a strong topic for study due to its variety of mechanisms for phase transitions. Ca_2RuO_4 is a Mott insulator that enters an insulating state below $T_{MI} = 357\text{K}$, which coincides with a structural phase transition due to a rotation in the RuO_6 octahedra in the crystal. In its higher temperature phase it acts as a conductor and a paramagnetic metal; this higher temperature phase can be accessed through pressure, applied current, and chemical doping. Across all methods of transition, we see a suppression of the typical antiferromagnetic ordering associated with Mott insulators, and a drastic decrease in resistivity to that of a conductor. Understanding this novel phase and how it can be achieved is the basis of this thesis, and μSR techniques will be used to uncover some of the mysteries in this material.

1.2 Material Context through Sr_2RuO_4

Setting the context for Ca_2RuO_4 cannot be done without reference to the other end member in the $\text{Ca}_{2-x}\text{Sr}_x\text{RuO}_4$ system. This is because one of the most researched topics in solid state physics is in unconventional superconductivity. Specifically, the last several decades of research on superconductivity has been centred around materials with strong electron correlations, looking at quantum critical points or transitional behaviour [1]. Sr_2RuO_4 is an example of an unconventional superconductor, and to explain its unconventional nature, we must take a brief look at conventional superconductors.

1.2.1 Conventional vs. Unconventional Superconductivity

To explain how unconventional superconductivity may occur, it is important to understand how conventional superconductivity works first. Superconductors universally possess Cooper pairs, which is a pair of electrons that form something similar to a Bose-Einstein condensate, meaning they will have either $S = 0$ for a singlet state, or $S = 1$ for a triplet state. Due to the fact that electrons as fermions anticommute, the antisymmetric singlet state is found with orbital angular momentum $L = 0, 2, \dots$, which represent s and d-wave orbitals, etc., and hence s and d-wave, etc., superconductivity in general. Similarly, the spin triplet state is present with orbital angular momentum of $L = 1, 3, \dots$, or in p and f-wave, etc., superconductivity.

Conventional superconductivity generally refers to s-wave superconductors, where s-wave Cooper pairs form a net attraction through electron-phonon interactions. The gap function, $\Delta(\mathbf{k})$, represents the order parameter in superconductors, and can be interpreted as the binding energy of a Cooper pair, or the minimum energy required to excite electrons to this state. The gap function in s-wave superconductors possesses the same phase in any direction of \mathbf{k} , and this is due to the fact that the only symmetry broken in s-wave superconductors is gauge symmetry when crossing T_c [1]. Gauge symmetry is violated as the U(1)-gauge symmetry seen in the Fermi surface is broken. This is due to the fact that Cooper pairs do not conserve the number of particles in the Fermi surface, instead transmuting some into a Bose gas or liquid. More symmetries are violated at higher angular momentum superconductivity, causing the sum of the gap function across all \mathbf{k} directions to be non-zero. Higher angular momentum states can occur in materials with strong Coulomb repulsion. This is because the strong Coulomb repulsion will cause the wavefunction of the Cooper pairs to possess an amplitude at non-zero wavevectors, as the electrons repel each other more strongly than normal [1]. Such a wavefunction can be described with higher angular momentum states, which gives rise to p, d-wave, or higher superconductors.

1.2.2 Evidence for Sr_2RuO_4 as a p-Wave Superconductor

Sr_2RuO_4 is the first layered perovskite superconductor discovered that possessed no copper ions in its lattice, separating itself from the famous d-wave cuprate class of superconductors [1]. It was not until NMR-based Knight shift experiments were performed that some evidence of triplet pairing began to show in the material. These measurements looked at the Pauli spin susceptibility, χ_s , and saw a temperature independent spin-susceptibility in the superconducting state, a finding which is only consistent with triplet pairing [2]. A similar temperature-independent susceptibility was also seen in spin-polarized neutron scattering experiments, reaffirming the result [3].

Relevant to this μSR -based thesis, important discoveries of additional symmetry breaking was found through use of μSR techniques. It was shown through zero-field experiments that the relaxation rate of muons below T_c increases above the standard relaxation, best modeled by an exponential, and longitudinal field experiments show suppression of this effect, making it a static effect [4]. A subsequent study which used lower quality samples with a lower T_c demonstrated that this extra relaxation is linked to the superconductivity in particular, ruling out the possibility that it is caused by a coincidental magnetic phenomenon appearing at a similar temperature [5]. This is interpreted as spontaneous fields, which results in time-reversal symmetry breaking, caused by supercurrents arising from variation in the order parameter near imperfections in the crystal [4].

Chapter 2

Background

2.1 Understanding Solid State Physics Models

Fundamentally in solid state physics, understanding real world phenomena seen in materials come from a basis in understanding the quantum interactions that take place inside a crystal lattice. With countless atoms in a given solid, this results in a many-body problem that would make programming many situations impossible with current technology. As such, laying the groundwork with simplified models and learning about their limitations and the information they give is crucial to building up understanding about any novel material. This section will focus on the Drude and Sommerfeld models, then expand into Hartree-Fock theory with this goal in mind.

2.1.1 Drude Model

The Drude model is one of the simplest models for understanding the crystal lattice, initially proposed to explain electrical and thermal conductivities in metals. We start with the idea that for every atom in a crystal lattice, there are positive ion cores made up of protons and neutrons, with electrons surrounding these ion cores equal to the number of protons in the cores. Most of these electrons are bound to the ion cores, laying in too low an energy band to be ionized and leave the atom, while the outermost electrons,

the valence electrons, are free to move around the solid in a random fashion. Critically, these electrons are seen as behaving classically instead of quantum mechanically. This is the idea of an “electron gas”, which is the initial basis for the model.

To expand the model into something that could generate useful results, more assumptions were made by Drude [6]. First, it is assumed that electrons that collide with ion cores simply bounce off without interaction. This means that electrons will simply continue bouncing off ions in directions following momentum conservation and the collisions are instantaneous. Second, the path of electrons is not in any way controlled by the presence of the ion cores, known as the “free electron approximation”. This means that there is no attractive force between the free electrons and the ion cores. Third, the path of electrons is not in any way controlled by the presence of movement of other electrons, known as the “independent electron approximation”. This means there is no Coulomb interaction between them, nor is the spin of the electrons ever considered. Fourth, there is a mean collision time for electrons before hitting an ion core, τ , known as the relaxation time approximation. And finally, the last main assumption is that the free electrons thermally equilibrate through collisions with ion cores.

All of these assumptions are quite severe, and cause some glaring inaccuracies in the natural results. That being said, there have been a few breakthroughs that have come of it. The primary great success of the model at the time was the theoretical agreement with the Wiedemann Franz Law, which sees that experimentally, most metals thermal conductivity to electrical conductivity ratio, κ/σ , is directly proportional to temperature, T . Using the Maxwell-Boltzmann Distribution Law,

$$f_B(v) = n \left(\frac{m}{2\pi k_B T} \right)^{\frac{3}{2}} e^{-\frac{mv^2}{2k_B T}} \quad (2.1)$$

and treating the electrons classically gives a result of

$$\frac{\kappa}{\sigma} = \frac{3}{2} \left(\frac{k_B}{e} \right)^2 T, \quad (2.2)$$

where k_B is the Boltzmann constant. This constant in front of the T approximately equals $1.11 \times 10^{-8} W\Omega/K^2$, the same order of magnitude of most metals. This comes out as a result of pure coincidence, however, as two errors in the calculation of the thermal conductivity were off by approximately 2 orders of magnitude in opposite directions. In fact, there are many drawbacks to such a simple model, and it is obvious that more needed to be known about the subatomic world to bring this model any further.

2.1.2 Sommerfeld Model

The Sommerfeld model is essentially the next step up from the Drude model in terms of physics of the crystal lattice. Decades after the Drude model was first conceived, it was discovered that electrons fell into a subatomic particle category of “fermions”, and that due to a phenomenon famously known as Pauli’s exclusion principle, electron locations were much more restricted than a Maxwell-Boltzmann distribution would imply. A new distribution naturally arose called the Fermi-Dirac distribution,

$$f(v) = \left(\frac{m^3}{4\hbar^3 \pi^3} \right) \frac{1}{\exp \left[\left(\frac{1}{2}mv^2 - k_B T_0 \right) / k_b T \right] + 1}. \quad (2.3)$$

Additionally, the field of quantum mechanics had exploded since, giving us the time independent Schrodinger equation to work with. Taking the same basic principles from the Drude model and adding in quantum mechanics and the Fermi-Dirac distribution, many useful outcomes occur. Starting with an independent electron that interacts with

a constant background electric potential driven by ion cores, which when set to zero we obtain a time independent Schrodinger equation of

$$-\frac{\hbar^2}{2m}\nabla^2\psi(\mathbf{r}) = E\psi(\mathbf{r}). \quad (2.4)$$

Solving this for energy, we have:

$$E(k) = \frac{\hbar^2 k^2}{2m}, \quad (2.5)$$

where k is known as the wavevector. Imposing Born-von Karman, or periodic, boundary conditions due to this being an effectively infinitely repeating crystal lattice causes k to equal certain values:

$$k_x = \frac{2\pi}{L}n_x, k_y = \frac{2\pi}{L}n_y, k_z = \frac{2\pi}{L}n_z, \quad (2.6)$$

with n_x, n_y, n_z being any integer. This combined with Pauli's exclusion principle means, that there are a only specific energy states electrons in the lattice can be in. As described in the Fermi-Dirac distribution, electrons will fill the lower energy states first, resulting in some electrons being forced into a higher energy state. These highest energy electrons are said to be at the Fermi energy, which separates the filled electron states from the unfilled excited states at absolute zero. The Fermi energy, E_F , is similar to [2.5](#), given by

$$E_F = \frac{\hbar^2 k_F^2}{2m}. \quad (2.7)$$

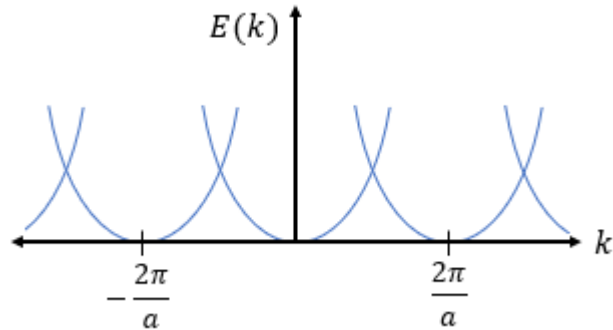


FIGURE 2.1: Each lattice site will possess its own energy curve as a result of the periodic boundary conditions, causing intersections between parabolae in the plot.

Taking periodic boundary conditions into consideration again, plotting 2.5 gives several overlapping parabolae, intersecting with the x-axis every $\frac{2\pi}{a}$, where a is the lattice constant, shown in 2.1.

Perturbation theory analysis at the intersections of these parabolae at $k = (1 + 2n)\frac{\pi}{a}$, where n is an integer, reveal that an energy gap will form, preventing the curves from intersecting. This means that at certain energies and wavevectors, an electron will have to gain a significantly greater amount of energy than normal to travel to the next excited state. Since mostly only the highest energy electrons, the ones at the Fermi surface, will ever become excited, the location of the Fermi energy in association with these gaps will be pivotal to understanding how electrons respond to excitation in a material.

Put simply, when the Fermi energy is between bands, and there is thus an energy gap to be overcome to excite any electrons, the result is an insulator. If the Fermi energy sits within a band, it is comparatively easy to excite valence electrons, allowing current to flow more easily, creating a conductor. Since the Fermi surface generally sits within the energy gap if the all electron orbitals are filled, and sits outside of the gap when they are not filled, the fact that Mott insulators exist, which do not have filled orbitals but are still insulating, goes unexplained. To understand Mott insulators, we must go over

further, and attempt to do away with the independent-electron approximation.

2.1.3 Hartree-Fock Theory

As Ca_2RuO_4 is believed to be a Mott insulator, background knowledge on the subject is necessary to understand the physics behind the material. As the phenomenon of the Mott insulator is not accounted for in Drude and Sommerfeld models, it is necessary to go beyond independent-electron approximations and discuss how electron potentials interact with each other. The primary model for doing this is Hartree-Fock theory, which begins with an altered Schrodinger equation below.

$$\sum_{j=1}^N \left(-\frac{\hbar}{2m_e} \nabla_j^2 \Psi - Ze^2 \sum_R \frac{1}{|\mathbf{r}_j - \mathbf{R}|} \Psi \right) + \frac{1}{2} \sum_{j \neq k} \frac{e^2}{|\mathbf{r}_j - \mathbf{r}_k|} \Psi = E\Psi \quad (2.8)$$

In equation (1), the first term here is the spatial derivative and the second is the potential between the ion cores and electrons, while the third term represents the electron-electron interaction. From here, we can attempt solutions with various wavefunctions, such as writing Ψ as a product of all N orthonormal electron wavefunctions,

$$\Psi(\mathbf{r}_1 \mathbf{s}_1, \mathbf{r}_2 \mathbf{s}_2, \dots, \mathbf{r}_N \mathbf{s}_N) = \psi_1(\mathbf{r}_1 \mathbf{s}_1) \psi_2(\mathbf{r}_2 \mathbf{s}_2) \dots \psi_N(\mathbf{r}_N \mathbf{s}_N) \quad (2.9)$$

This gives the ‘‘Hartree equations’’ out of the Schrodinger equation,

$$\left(-\frac{\hbar}{2m_e} \nabla_j^2 + U_{ion}(\mathbf{r}) + e^2 \sum_{j \neq i} \int \frac{|\psi_j(\mathbf{r}')|^2}{|\mathbf{r} - \mathbf{r}'|} dr' \right) \psi_i(\mathbf{r}) = E_i \psi_i(\mathbf{r}). \quad (2.10)$$

Solutions to these are generally found through guessing the wavefunction forms, then iterated upon to alter the wavefunctions. There are two main problems with the Hartree equations. First, Ψ violates the Pauli exclusion principle, as Ψ should change sign

with respect to the interchange of any two electrons. Second, the electrons interact only with the average field generated by the remaining electrons, neglecting that each electron should individually interact with each other electron, causing correlation. The first problem is solved simply by using the Slater determinant as the trial wavefunction instead of equation (2). This results in the Hartree-Fock equations,

$$E_i\psi_i(\mathbf{r}) = -\frac{\hbar^2}{2m_e}\nabla^2\psi_i(\mathbf{r}) + U_{ion}(\mathbf{r})\psi_i(\mathbf{r}) + \sum_{j\neq i} \int \frac{e^2|\psi_j(\mathbf{r}')|^2}{|\mathbf{r}-\mathbf{r}'|}d\mathbf{r}'\psi_i(\mathbf{r}) - \sum_{j\neq i} \int e^2\frac{\psi_j^*(\mathbf{r}')\psi_i(\mathbf{r}')}{|\mathbf{r}-\mathbf{r}'|}d\mathbf{r}'\psi_j(\mathbf{r})\delta_{s_j s_i}. \quad (2.11)$$

The fourth term here is the exchange term, which is nonzero for parallel spin electrons, meaning the motion of the electrons with parallel spins are correlated. Thus, in these equations there is inclusion of spin correlation (exchange) effects, but not Coulomb repulsive correlation effects, as the second issue with the Hartree equations is still unresolved here. From these, the term correlation energy can be used as the energy difference between the Coulomb and exchange correlations.

From this derivation, one can make further simplifications in order to look at specific interactions or situations. The Jellium model is a good example of this. The Jellium model, or the Hartree-Fock theory for free electron gases, puts the electron-electron interactions at the forefront, taking the periodic lattice and replacing it with a constant positive background potential. Now, the wavefunction of orthonormal plane waves as derived in [7] can be used to give a solution for the energy levels in such a situation,

$$E(k) = \frac{\hbar^2 k^2}{2m_e} - \frac{2e^2}{\pi k_F} F\left(\frac{k}{k_F}\right) \quad (2.12)$$

where,

$$F(x) = \frac{1}{2} + \frac{1-x^2}{4x} \ln \left| \frac{1+x}{1-x} \right|. \quad (2.13)$$

The first term of equation (5) shows the energy of an electron in this situation, and the second term represents the effects of electron-electron interactions. Evidently, since $F(\frac{k}{k_F})$ is always positive, this serves to reduce the overall energy in the energy levels. Having lower energy electrons we will see can cause interesting phenomena to occur, such as Mott insulation.

2.2 Mott Insulators

Phenomenologically, Mott Insulators most commonly appear as metals with an electronic phase transition from an insulator to a conductor at some critical temperature, T_{MI} . In order to understand this phenomenon on a basic level, consider a lattice of monovalent atoms, which correspond to a half filled band picture. As Roy writes, electrons jumping to another lattice site is possible, assuming the outermost atomic orbitals between two adjacent sites partially overlap [7]. The energy gained through jumping to an adjacent site is balanced against the Coulomb repulsion that would be created to determine favourability of the jump. As the interatomic distance increases, the energy gain from the jump is minimized and the Coulomb repulsion becomes dominant, effectively restricting electrons to their own atoms. This of course, prevents current from flowing through the material as electrons are not “free”, creating a Mott Insulator. In summary, while band insulators simply have no open states for electrons to take in neighbouring sites, causing their restriction, Mott insulators would be metals in absence of perturbations, but they have strong enough electron repulsion or large enough interatomic spacing to strongly discourage intersite travel of electrons, thus insulating them.

2.2.1 Hubbard Bands

To further explain the insulator-conductor transition, let us look at a similar situation in which we have a solid with an infinite lattice constant as done in “Mott Insulators”, a textbook by Roy [7]. In it, he represents the electron energy of the solid in terms of the number of lattice sites with one and two electrons, N_1 and N_2 , respectively, the binding energy of an electron onto the solid, t_0 , and the Coulomb interaction energy of two electrons located at the same lattice site, U . This gives a total electron energy of

$$E = N_1 t_0 + N_2 (2t_0 + U), \quad (2.14)$$

and now considering solids with one valence electron, $N_1 = N$, $N_2 = 0$, and each of the N ground state electrons have energy t_0 , resulting in a stable configuration with localized electrons throughout the solid. Additionally, the electrons will, for reasons explained in the next part, order into an antiferromagnetic ground state. If we now shrink the lattice, giving it a finite lattice constant, and add one electron to the lattice, it can be placed at any of the $N/2$ lattice sites with an electron of opposite spin to it. The other half of the sites are of course forbidden due to Pauli's exclusion principle. We know with help from equation 2.14 that this adds $t_0 + U$ electron energy to the lattice site. But since the lattice constant is finite, there is also a finite interaction between this new electron and all the $N/2$ sites with an electron of opposite spin. This results in a splitting of the energy into an energy band centred at $t_0 + U$. If one now goes through the same argument for the removal of an electron, a similar band is formed centred at t_0 . There will be a gap between these bands as long as the bandwidth is smaller than the Coulomb interaction energy of intrasite electrons, U , as seen in the diagram in 2.2. This gap begins to vanish as the lattice constant shrinks, as this will increase the width of the Hubbard bands until they overlap. With the bands fully overlapped, the solid can be appropriately described using typical band theory, and the result is a half-filled band

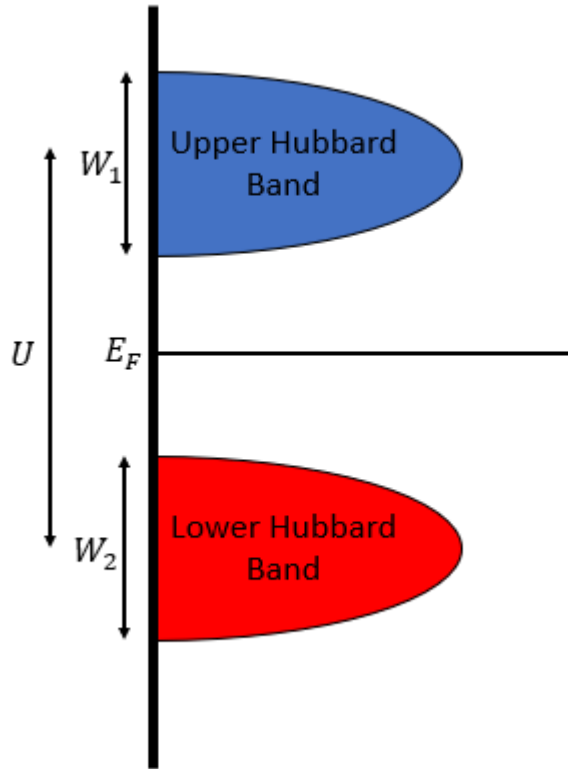


FIGURE 2.2: A diagram of the Hubbard Bands in a Mott insulator. The y axis is electron energy, and the x axis is electron density of states. Note that the Fermi energy is between bands, creating a large energy gap for electrons to overcome.

and a paramagnetic metal.

2.2.2 Antiferromagnetic Ordering

As alluded to above, Mott Insulators at ground energy will order antiferromagnetically. In order to demonstrate this, we can once again look to a hypothetical setup in Roy's "Mott Insulators" on Mott-Heisenberg insulators [7]. Starting with a Mott insulator in its insulating regime, we can look at the exchange interaction between the localized spins to determine whether antiferromagnetic ordering is stable for such a material. Taking the Mott insulator as a square lattice and assume antiferromagnetic ordering,

the ground state with no hopping between points is denoted by $|X_0\rangle$, with corresponding energy E_{X_0} . The excited state $|X\rangle$ occurs when electrons tunnel to neighbouring sites which, despite being localized, is still known to occur as seen in 2.3. From second-order perturbation theory thus comes

$$E = E_{X_0} + \sum_{X_0} \frac{|\langle X_0 | H_{\text{hopping}} | X \rangle|^2}{E_{X_0} - E_X} = E_{X_0} - \frac{Nzt^2}{U} \quad (2.15)$$

where t is the perturbative amplitude representing the likelihood of hopping from one lattice site to its neighbour, N is the number of lattice sites, z is the number of nearest neighbours, and U is still the Coulomb interaction energy between two electrons at the same lattice site. Since the spin states of all electrons is conserved, if the initial orientation here was ferromagnetic in nature, then no hopping could occur. This would lead to a higher energy configuration, thus leading one to believe that antiferromagnetic ordering to be preferable.

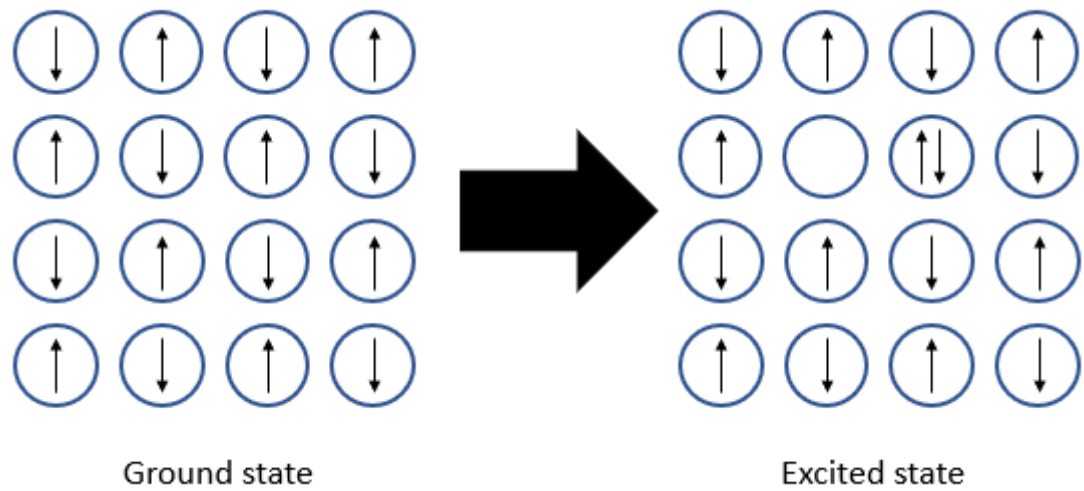


FIGURE 2.3: A diagram of the antiferromagnetic ground state in a Mott insulator being able to accommodate a simple excited state, where a ferromagnetic Mott insulator would not be able to from Pauli's exclusion principle.

Chapter 3

Ca₂RuO₄ Research

3.1 Ca₂RuO₄ phases

Ca₂RuO₄ is an end member of the isoelectronic Ca_{2-x}Sr_xRuO₄ system, with the other end being the well-researched p-wave superconductor Sr₂RuO₄ [1]. Ca₂RuO₄ was first reported in 1997, where two phases were synthesized, and crystal structures analyzed [8]. The two main phases are differentiated primarily through a difference in c-axis lengths, the longer of which is denoted the “L” phase, and the shorter is denoted the “S” phase, both seen in 3.1. Both phases are orthorhombic, possessing a very similar structure to its layered perovskite counterpart Sr₂RuO₄, but with tilts in the RuO₆ octahedra that distort the lattice [9].

The aforementioned tilts in RuO₆ octahedra prevent the material from taking the more symmetrical, tetragonal K₂NiF₄ structure of the I4/mmm space group, and distort the lattice in two critical ways. First is a rotation about the c-axis, similar to Sr₂IrO₄, which is of space group I4₁/acd [10]. Second is another rotation, this time about an axis in the ab-plane, which prevents a tetragonal structure from existing [10]. These rotations put both L and S-Ca₂RuO₄ in the orthorhombic Pbc_a space group. As we will see later, the S phase is electrically insulating while the L phase is not, despite being the

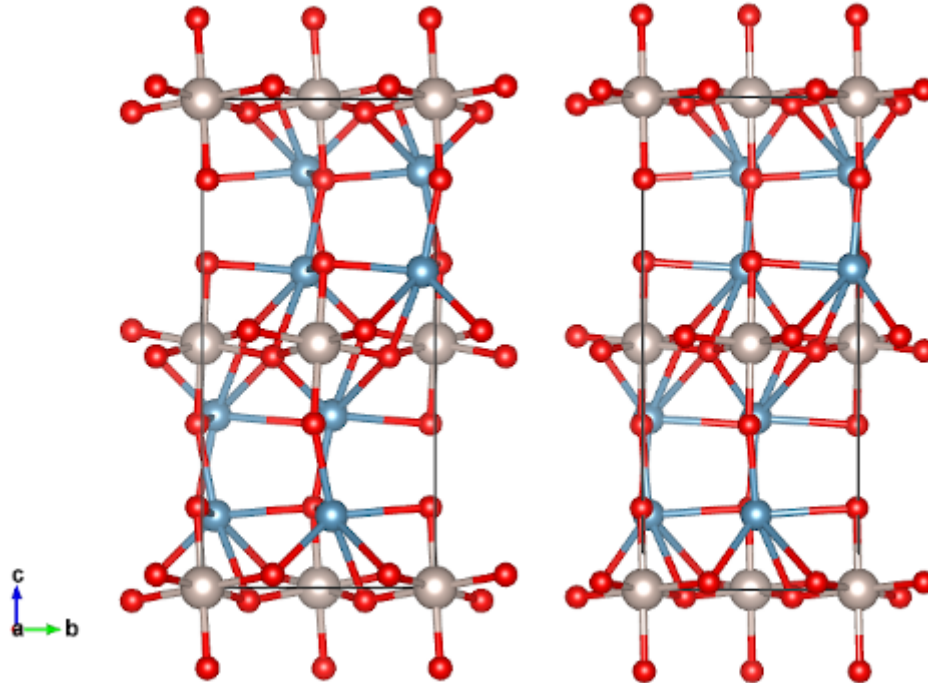


FIGURE 3.1: Pictured are the short S phase (left) and long L phase (right) of Ca_2RuO_4 , adapted from the data collected by [9]. Note the L phase possesses less distortion in the RuO_6 octohedra, causing its c axis to grow slightly.

same material with the same space group.

A transition between L and S- Ca_2RuO_4 can be induced through various means. The first method is through temperature, which was first reported on in Friedt et al.[9]. Here, analysis of the RuO bond lengths showed that the transition temperature between the L and S phases was found to be at approximately 357K in a first order phase transition, as seen in 3.2. The same paper created a phase diagram of $\text{Ca}_{2-x}\text{Sr}_x\text{RuO}_4$, demonstrating that the L and S phases can also be transitioned between through chemical substitution, as $0.05 < x < 0.2$ yields a stable L phase at room temperature [9].

Pressure has also been found to induce a phase transition between the L and S phases, studied in depth by Steffens et al. [11]. In this paper, it was found that at

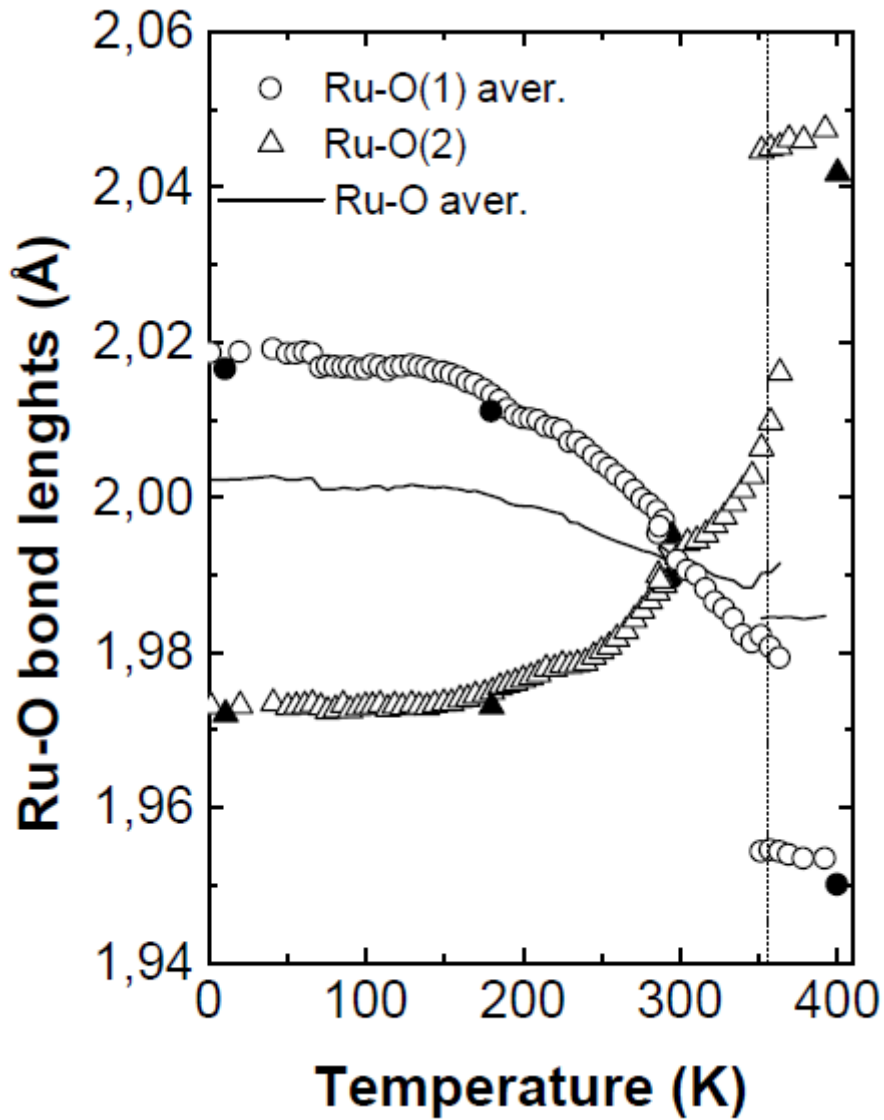


FIGURE 3.2: A plot of RuO bond lengths demonstrating the Mott transition temperature. The bifurcation point in the data at approximately 357K is the clearer transition point [9].

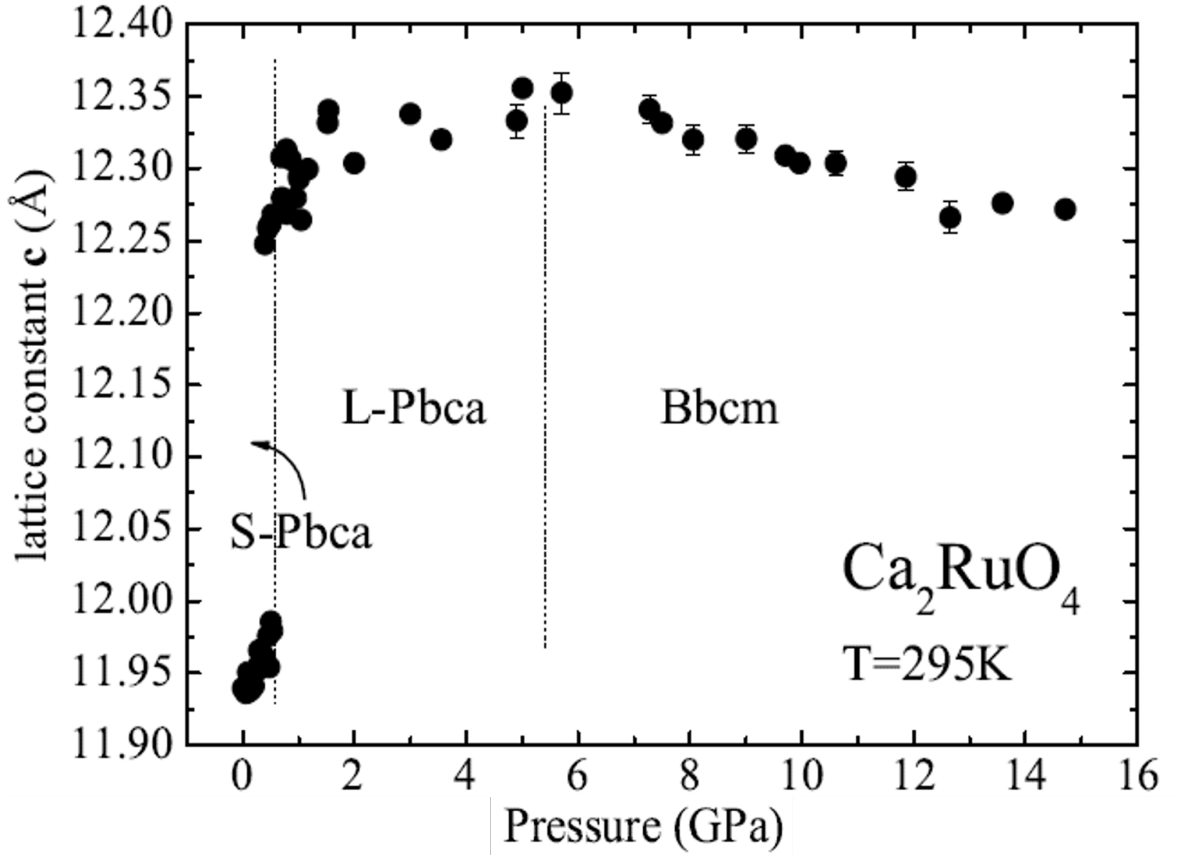


FIGURE 3.3: A plot of the c-axis lattice constant lengths demonstrating the pressure activated Mott transition. The transition at 0.5GPa indicates a shift from the Mott insulating S-phase to the metallic L-phase, and the phase above 5.5GPa is a higher symmetry structure [11].

room temperature 0.5GPa of pressure cause a first order structural transition from S to L- Ca_2RuO_4 , as seen in 3.3. The magnetic ordering of both phases was analyzed, demonstrating that in S- Ca_2RuO_4 there is antiferromagnetic ordering, $T_N=112\text{K}$, and in L- Ca_2RuO_4 there is ferromagnetic ordering, $T_C=25\text{K}$. S- Ca_2RuO_4 was also determined to be a Mott insulator, while L- Ca_2RuO_4 was found to be metallic.

Additionally, a third phase of Ca_2RuO_4 was discovered under high enough pressure (5.5GPa at room temperature) or higher temperature (650K at 0GPa). This phase comes as a result of the RuO_6 octahdra in L- Ca_2RuO_4 rotating to enter a higher symmetry

space group, Bbcm [11]. Magnetic ordering of this phase was not seen as high enough pressures to maintain the higher symmetry phase at lower temperatures could not be achieved [11].

Finally, and most critically for this thesis, it was shown that the phase transition between L and S-Ca₂RuO₄ can be induced by a modest electrical current [12]. Electric field-induced Mott insulators are not very common and tend to have a very high threshold fields for transition, but this has been shown not to be the case for Ca₂RuO₄ [12]. In fact, a transition between the L and S phases can take place with an electrical field as low as 40V/cm [12]. This extends from low temperature conditions to room temperature, giving relative stability to the phase when under a relatively low current [12].

Studies into Ca₂RuO₄ are useful to contrast with Sr₂RuO₄, but the phase transitional properties of Ca₂RuO₄ are also of particular interest to research of bolometric devices. Such devices rely on Ca₂RuO₄'s ability to undergo first order transition between an insulating and a conducting phase through various means, but particularly through application of a modest current.

3.2 Research on Ca₂RuO₄ Magnetic and Transport Properties

3.2.1 Magnetization Data

A typical magnetic Mott insulator will enter an insulating state below a temperature T_{MI} , and below this an antiferromagnetic transition at a Néel temperature, T_N . We see that pure Ca₂RuO₄ behaves in this typical nature, as reproduced in Figure 3.4 [13]. It is notable that the applied field parallel to the c-axis results in higher magnetization than the field applied perpendicular to the c-axis, highlighting the magnetic anisotropy present in the material. This indicates that the easy axis of magnetization rests in the

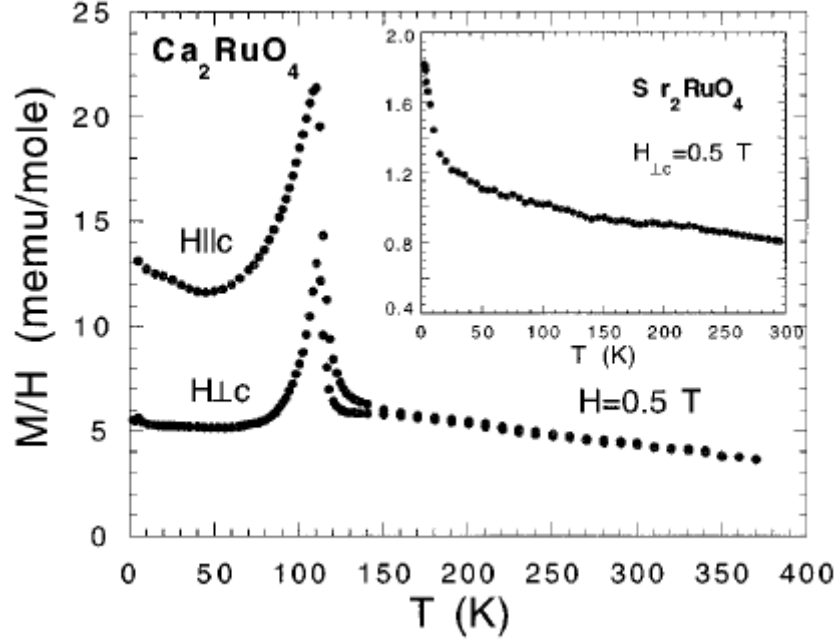


FIGURE 3.4: Magnetic susceptibility data for $0.5T$ fields applied both along the c -axis, and perpendicular to the c -axis, from [13]. A inset comparison to the magnetization of Sr_2RuO_4 is also given, highlighting their differences.

ab-plane. The Néel temperature is 110K, but [13] was unable to fit the high-temperature susceptibility to a modified Curie-Weiss law. They go on to speculate that this is due to structural distortions near the Néel temperature, resulting in an altered Ru-O-Ru bond angle [13]. They justify this speculation citing other ruthenates, where this bond angle is a sensitive determinant of ordered moments and $4d-2p$ orbital overlap, and that Ca_2RuO_4 crystals have been known to shatter near the Néel temperature, suggesting a potential strain on the crystal from a structural distortion [14].

3.2.2 Resistivity Data

Early resistivity data on Ca_2RuO_4 suggests that the material behaves as a rather typical Mott insulator while under low currents and ambient conditions, as seen in figure 3.5 [13]. Resistivity increases exponentially as temperature decreases, showing non-metallic

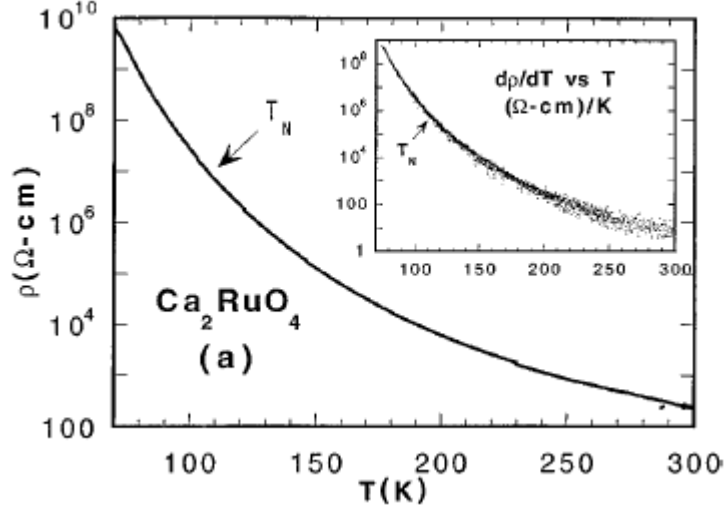


FIGURE 3.5: Resistivity data for Ca_2RuO_4 under very low applied current demonstrating an exponential increase in resistivity as temperature decreases, from [13]. The inset and the arrows pointing out the Néel temperatures show that there is no anomaly in the data or its slope at the transition temperature.

behaviour that one would expect from a Mott insulator. Additionally, no anomalies were seen in resistivity at the Néel temperature for either the resistivity or its derivative [13].

Resistivity measurements showed that an applied current could suppress the Mott gap in Ca_2RuO_4 . Seen in 3.6, an increase in applied current causes a clear decrease in the resistivity of the material across all temperatures [15]. There is still a nonmetallic trend seen in the resistivity, as the resistivity still increases as temperature decreases, but the fact that an increase in current serves to flatten the curves and lower the resistivity at low temperatures suggests that the Mott gap is closing and the system is transitioning to a metallic state.

3.3 Mott Insulator Transition

As discussed in the section on Mott insulators, one typical mechanism in which the Mott gap is closed is through temperature, giving the critical temperature T_{MI} , above which

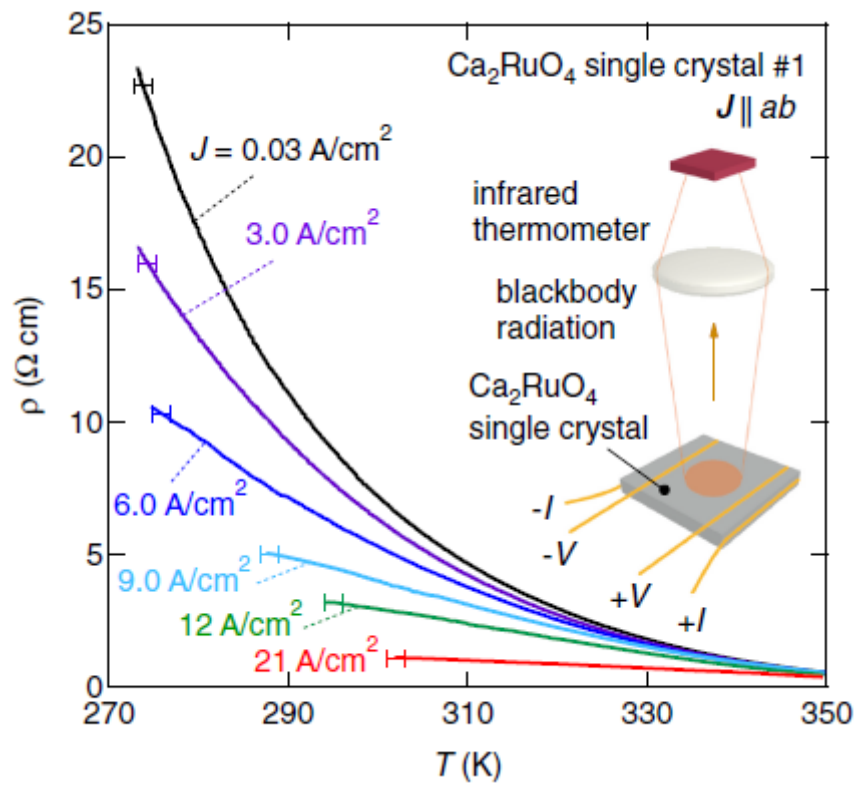


FIGURE 3.6: Resistivity data for Ca_2RuO_4 under several current densities for relatively high temperatures. As current increased, resistivity decreased across all temperatures [15]

the Mott gap closes and the system typically behaves as a paramagnetic metal. From discussion of the phase switching abilities of Ca_2RuO_4 , this is obviously not the only way to do so. In general, the methods for transitioning are through controlling the Hubbard band bandwidth or through band filling with more electrons. Pressure is a good method for expanding the bandwidth of the material, as reducing the lattice constant by external pressure will increase the overlap between neighbouring site electron orbitals, making intersite travel easier.

Chemical substitution and electrical current are methods of inducing an increase in the charge carrier density in the sample, causing free electron flow to be more permissible [7]. Chemical substitution for oxides partially replaces a cation with a different cation that can more readily provide charge carriers. This effectively reduces the electron Coulomb repulsion for certain electrons in the lattice, closing the Mott gap and allowing easier current flow. Running an electrical current is not so simple, as the specific mechanism varies and is more complex.

Okazaki et al. in 2013 investigated the nature of the suppression of the Mott gap in Ca_2RuO_4 and put forward a theory of its mechanism[15]. They suggested that a Jahn-Teller distortion is responsible for the gap suppression. The Jahn-Teller effect tells us that when there is a degenerate electronic ground state in a material, the material will alter its crystal structure in order to remove this degeneracy and lower its overall energy. For Ca_2RuO_4 , strong Coulomb repulsion among $4d$ electrons and known tetragonal crystal-field splitting from flattened RuO_6 result in d_{xy} orbital ordering in the insulating phase. Excited charge carriers from an applied current will thus want to decrease the degenerate orbital polarization, causing distortions in the RuO_6 octahedra and ending with the destruction of the Mott gap.

This theory has since been further expanded upon by Zhao et al. in 2019, who also suggest that the Mott insulating state is orbitally ordered and that the Jahn-Teller

effect is what causes the distortions in the octahedra [16]. They suggest that the orbitally ordered insulating state possesses an average polarization of $n_{xy} = 1.5, n_{yz} = 1.5, n_{xz} = 1.5$ for the t_{2g} orbitals. This ratio is gradually skewed with the application of current as n_{xy} approaches 1.0 (half-filled) due to this orientation being most favourable for electron hopping, reducing the tilt of the octahedra and transforming the structure towards the L-phase which closes the Mott gap [16].

3.4 Current-Induced Magnetic Properties of Ca_2RuO_4

As discussed previously, low current measurements of Ca_2RuO_4 show that it behaves as a typical Mott insulator, with the exception of its rather unique structural phase transition corresponding to its T_{MI} . This makes Ca_2RuO_4 a paramagnetic metal above $T_{MI} = 357\text{K}$, and an insulator below, with an antiferromagnetic ordering temperature of approximately 110K. Investigations into Ca_2RuO_4 's electrical and magnetic properties have proven difficult across the years, as maintaining a low temperature and accurate thermometry under even modest current can at times be quite a daunting task. One of the first papers to identify that current could switch Ca_2RuO_4 to its conducting state was Nakamura et al., which demonstrated that a modest electric field could switch the material. Here, they noted that the switch is coupled with a structural transition to L- Ca_2RuO_4 , and that this state could be maintained after the switch with an even weaker current [12].

A comprehensive neutron scattering paper by Zhao et al. in 2019 sheds some light on the situation through collection and analysis of Ca_2RuO_4 's magnetization [16]. Applying a current below $0.15\text{A}/\text{cm}^2$ yields slight suppression of the antiferromagnetic ordering below 110K, reverting to its paramagnetic state. It was found that upon applying a current exceeding $0.15\text{A}/\text{cm}^2$, sub-80K temperatures give a nonequilibrium orbital state, distinct from the paramagnetic state above it on a phase diagram. The authors claim

that in this current regime, resistance anomalies can be seen, dependent on whether the current in the Ca_2RuO_4 samples was ramped up slowly (“trained”) or instantaneously (“untrained”). Untrained samples report a large jump in resistivity at approximately 90K, larger than any jump in the trained samples.

Resistivity has also been seen to be significantly impacted by applied current. As an insulator, Ca_2RuO_4 has a notably high resistivity under normal circumstances. This does not hold true under larger currents, as applying currents in the range of $0.15\text{A}/\text{cm}^2$ decreases the sample’s resistivity by orders of magnitude. The decrease in resistivity is gradual, suggesting that there is no first order transition to the conducting state through this mechanism. It should also be noted that resistivity increases with a decrease in temperature regardless of the applied current, which is not particularly unusual but puts a limit on how low a temperature can be achieved with smaller currents without a large voltage.

3.5 Spin-Orbit Coupling in Ca_2RuO_4

Orbital degrees of freedom refers to a material’s orbital degeneracy and orientational anisotropy, which are fundamental to its charge and spin. Ca_2RuO_4 as well as Sr_2RuO_4 possess four electrons in three nearly degenerate $4d t_{2g}$ orbitals, making the orbital degrees of freedom a property that could potentially control lattice effects through orbital ordering where localized occupied orbitals form a regular pattern, and Jahn-Teller distortions [17]. In addition, the spin-orbit interaction in $4d$ shells are quite large, causing the orbital angular momentum and spin angular momentum to potentially couple quite strongly. Since Ca_2RuO_4 is a Mott insulator and thus has localized $4d$ electrons, and is related to Sr_2RuO_4 in which $4d$ electrons play a pivotal role in its superconductivity, it is an interesting material for study of its orbital degrees of freedom and spin-orbit coupling.

It can be seen from x-ray absorption spectroscopy that orbital population changes massively between 90K and 300K [17]. This corresponds with a change in crystal structure within this temperature range, contracting the c-axis by 2.5%. To explain this, Mizokawa et al. performed circular polarized photoemission measurements and Hatree-Fock calculations, revealing that the $4d$ band possesses a large orbital angular momentum and Ca_2RuO_4 possesses a strong spin-orbit interaction [17]. It stands to reason that a large spin-orbit interaction combined with a rather small distortion in the RuO_6 octahedra would make up for this discrepancy in orbital population change, giving strong evidence that Ca_2RuO_4 possesses strong spin-orbit coupling.

3.6 Titanium dopings in Ca_2RuO_4

It must be noted that this overview of Ca_2RuO_4 is centred primarily around pure Ca_2RuO_4 samples. As this thesis exclusively uses 1% Ti doped Ca_2RuO_4 in its procedures, it is important to establish the effects that this will have on the system. The primary purpose of the 1% doping is that such a small amount is enough to provide some stability to the lattice and significantly reduce the fragility of the material, and this will be further explained in Chapter 5. This does, however, slightly reduce structural distortions in the material and considering that that is the primary cause of most of its interesting properties, the exact effects should be quantified [18].

Thankfully, a thorough analysis of the effects of Ti doping in Ca_2RuO_4 has been reported in Kunkemoller et al. in 2017 [18]. In this article, it was reported that 1% Ti doped Ca_2RuO_4 is very similar to pure Ca_2RuO_4 and that it is only the 10% Ti doped tested that showed any demonstrable difference in most physical properties from neutron scattering, resistivity, and magnetization data [18]. It was seen that 1% doped Ti possessed a T_{MI} 4K lower in temperature than the pure sample, agreeing with the idea what the doping provides slight stability to the lattice [18]. The stabilizing effect

can be explained by referring back to the distortions in the crystal lattice. The main source of distortion in the crystal lattice is from the RuO_6 octahedra, where the higher temperature L-phase possesses less distortion than the S-phase which flattens along the c-axis. Replacing some of the Ru atoms here with smaller Ti atoms would allow for a slight decrease in the distortions here, slightly stabilizing the conducting phase.

Physical properties of samples with dopings of 0% Ti, 1% Ti, and 10% Ti collected by Kunkemoller et al. can be seen in 3.7. It can be seen that 10% Ti doping causes a different transport properties altogether for high temperatures, and the authors state that a T_{MI} could not be seen above 80K, in stark contrast to pure Ca_2RuO_4 [18]. In comparison, the 1% doping is far more similar to pure Ca_2RuO_4 in resistivity. The primary difference is the resistivity of the 1% doped sample is an order of magnitude lower than pure Ca_2RuO_4 , but the overall shape of the resistivity curve is maintained. It should be noted that the lowered resistivity is beneficial for current-based experiments on the material such as the one presented in this thesis, as this helps lower power dissipation for the same current and the requirements for the max voltage on the power supply are lowered significantly, enabling a wider range of currents to be tested.

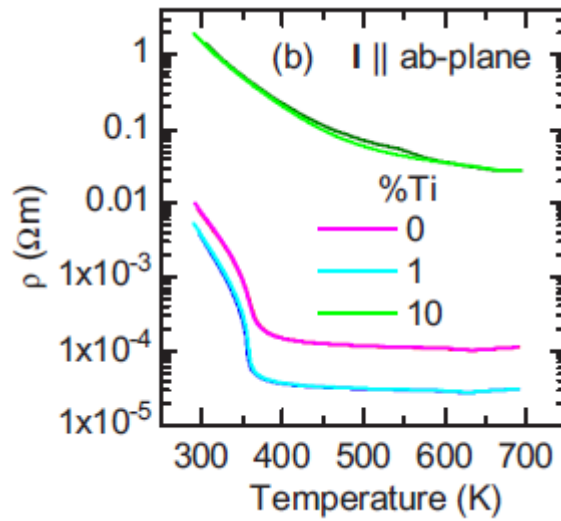


FIGURE 3.7: Resistivity data for pure and partially Ti doped Ca_2RuO_4 for relatively high temperatures. pure and 1% doped Ca_2RuO_4 are similar in shape and while in the conducting phase are an order of magnitude apart in resistivity, while 10% doping shows entirely different resistivities [18].

Chapter 4

μ SR Techniques

4.1 Muon Creation and Decay

To understand a μ SR study on Mott insulator Ca_2RuO_4 , we must first discuss μ SR and what it can do to investigate the interesting properties of Ca_2RuO_4 . μ SR, or “Muon Spin Rotation/Relaxation/Resonance”, uses muons to probe materials and determine the local fields at particular muon sites in the crystal lattice. Muons, being approximately $\frac{1}{9}$ the mass of a proton and charged, are a useful alternative to neutron diffraction as the charge allows for muons to be captured by the lattice and “sit” in the crystal lattice until its decay instead of diffracting off the lattice as neutrons do.

The production of muons for a beamline are typically generated first through the acceleration of high energy protons in an accelerator. These protons are fired at a target sheet of material with a low atomic mass with the purpose of producing pions, where one possible pion producing reaction is

$$p^+ + p^+ \rightarrow \pi^+ + p^+ + n. \quad (4.1)$$

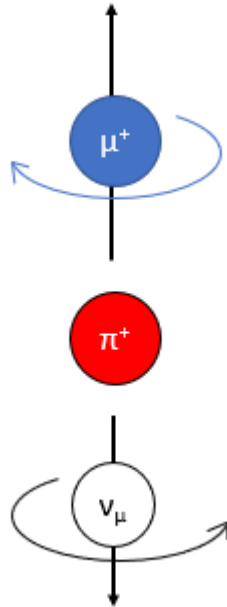


FIGURE 4.1: Newly created pions naturally decay into muons and neutrinos. Conveniently for μ SR research, the spin vectors of the resulting neutrino and muon will be antiparallel with their momentum.

Pions will naturally decay via the weak interaction into muons after approximately $0.026\mu s$, following

$$\pi^+ \rightarrow \mu^+ + \nu_\mu, \quad (4.2)$$

where ν_μ is a muon neutrino. From here, useful identifications can be made related to the newly generated muon's spin from momentum conservation observations. Pions are zero spin particles, while muons and neutrinos are spin-1/2 particles. This means that, when looking at pions that decay while at rest, it can be expected that the muon and neutrino created with have opposite momentum as well as opposite spins. This phenomenon can be coupled with the incredibly useful fact that neutrinos have their momentum always antiparallel to their spin vector. This requires that muons spins are

similarly antiparallel, as seen in 4.1, and if pions that decay at rest can be selected for (in other words, pions that stop in the target), then a beam of 100% spin-polarized muons can be generated.

This beam can now be aimed towards a sample of interest, where a thick enough sample will allow for the muons to stop in the lattice before they decay. The muons at the TRIUMF beamline possess a maximum momentum of $p_{\mu}^{max} = 29.8MeV/c$, which causes them to stop in approximately $140mg/cm^2$ of areal density, allowing for the stopping in a sample lattice to occur. Muons will decay by themselves via the weak interaction with a lifetime of $\tau_{\mu} = 2.2\mu s$ as

$$\mu^{+} \rightarrow e^{+} + \nu_e + \bar{\nu}_{\mu}, \quad (4.3)$$

where the positron and neutrinos will travel in directions dependent on the distribution of momentum between the three particles. In general, this decay process violates parity, as the positron will have a significant preference for taking on a momentum correlated with the muon spin vector at the time of decay, as seen in 4.2. If there are magnetic moments present in the sample, they can be probed simply through the detection of positrons as they decay in any direction.

4.2 Asymmetry Plots

A clock that starts when a muon enters the sample and ends when a positron hits the detectors placed in front of and behind the sample, coupled with the fact that the muon spin direction is known before it enters the sample, will paint a picture of the local magnetic field at the muon sites when sufficient positrons are detected. With a setup similar to the schematic in 6.2, a muon that decays in the sample will preferentially decay early, before it has time to precess from the local or external magnetic field. This

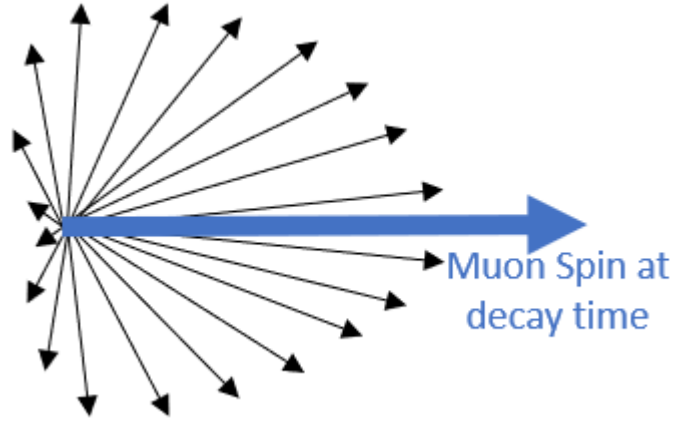


FIGURE 4.2: Positrons will be ejected preferentially in the direction of the spin of the muon from which it is created. Here, the blue arrow is the muon spin at time of decay and the black arrows are potential ejection directions, with larger arrows representing more likely outcomes.

causes it to preferentially hit the back detector. For slightly larger decay times, the muon will have precessed towards the front sensor before decaying, causing the ejected positron to preferentially hit the front detector. Asymmetry plots, where

$$A(t) = \frac{N_B(t) - N_F(t)}{N_B(t) + N_F(t)}, \quad (4.4)$$

and N_B and N_F are the total number of positrons detected as a function of time on the back and front detectors, respectively. The frequency is dependent on the strength of the magnetic field felt by the muon, allowing even small local moments near the muon sites in the lattice to be detected and studied. This makes the asymmetry a good measure of the time dependent spin polarization of the muon, making it a good probe of local fields in a sample. In a paramagnetic system, the asymmetry plot will simply be a relaxing exponential curve in most cases, relaxing the polarization as random fluctuations cause the muons to bias slightly more towards the forward sensor as time goes on. In a magnetically ordered system, the result will usually possess a similar exponential due to

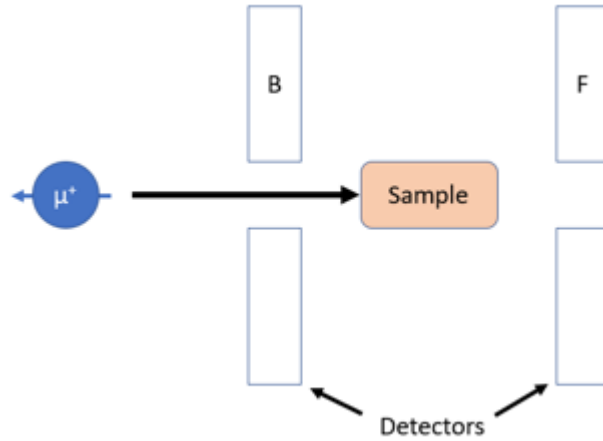


FIGURE 4.3: A basic diagram of inside the cryostat on the muon beamline. When a muon enters the sample chamber, it has a chance to stop in the sample before decaying, changing its spin in accordance with the local magnetic fields at the sample's muon site. Here rests six counters (only back and front counters labelled) that surround the sample rod, allowing for positron detection for a variety of muon spin configurations. In general, the front and back counters are used for most zero field runs, while the left and right are mostly used when a transverse field is applied to the sample chamber. The up and down counters (not pictured here) are most commonly used in spin rotated mode, where the muon spin polarization is altered to point upward instead of backward.

the background signal depending on the sample apparatus, but will possess an oscillating perturbation on this curve associated with the muons that stop in the sample.

μ SR is a powerful tool for probing local magnetic fields due to the muon's ability to sit at a specific site in the crystal lattice and give information on the internal field distribution even without an applied external field. As a muon precesses in a sample, the statistical peaks of muons hitting the back and front sensor give the full precession an accurate timeframe, given enough muons. Simply taking a Fourier transform of an asymmetry plot will reveal the field distribution experienced by the muons.

In some systems, muons will have multiple stopping sites in a crystal lattice, each with their own magnetic field. The results when this occurs will introduce additional

frequencies into the data. In a magnetically ordered, zero field measurement, this would normally indicate that the magnetic moments in the material are far enough apart to give an inconsistent internal field. A Fourier transform again may uncover if there is a second oscillation, as it will reveal which frequencies are present in the collection of muons.

Chapter 5

Synthesis of Ca_2RuO_4

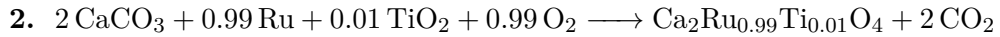
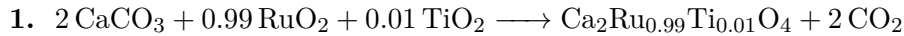
5.1 Limitations of Crystal Growths and Experimentation

Ca_2RuO_4 possesses a structural phase transition above room temperature that couples with its transition between a metal and a Mott insulator. This transition is arguably what gives the material several interesting properties, but also gives rise to the system's largest complication in synthesis and testing. Upon cooling after growth, Ca_2RuO_4 single crystals have a strong tendency to fracture into $\sim\text{mm}^3$ sized pieces or smaller, too small for testing in experimental techniques that use bulk samples such as μSR or neutron scattering. This is caused by the strain the first order phase transition causes on the crystal lattice. Fortunately, dopings of various metal ions have been shown to increase stability or even make the phase transition second order depending on the substitutions used [18, 19]. From this, it has been shown that dopings of 1% TiO_2 for RuO_2 (in other words, $\text{Ca}_2\text{Ru}_{0.99}\text{Ti}_{0.01}\text{O}_4$) increase the crystal's stability dramatically, increasing the potential crystal size by several times in all dimensions, and making them more viable for testing in μSR experiments, of particular interest in this project [18]. In addition, applying a phase-switching current to a pure Ca_2RuO_4 crystal can ordinarily only be done once as the crystals will often break or fracture when returned to the insulating state [20]. This is not true for the titanium doped crystals, as the extra stability has

allows samples to continuously be injected with relatively-sized currents during testing. Perhaps most importantly, 1% titanium dopings has been shown to have little impact on magnetic properties and ordering temperatures, making them perfect for use in studies on Ca_2RuO_4 single crystals [18].

5.2 Synthesis Attempts

Single crystal synthesis of Ti-doped Ca_2RuO_4 was attempted using an optical floating zone image furnace at McMaster University. Powders were first stoichiometrically prepared according to one of two pathways used over the course of the synthesis.



Both reactions were attempted throughout the synthesis attempts as RuO_2 powder ran low. Reactants were mixed in a mortar and pestle until the mixture was uniform in colour and texture, then the powder was hydrostatically pressed into rods and annealed in a high temperature furnace at 1700K. For reaction 1, annealing took 24 hours total at temperature, with one regrinding step halfway, and no difference in air or Ar atmosphere was seen. Reaction 2 was found to take 12 hours total at the same temperature with no regrinding step in a normal air atmosphere to produce the proper phase.

We made several attempts at growing 1% Ti doped Ca_2RuO_4 in the optical floating zone image furnace at McMaster, but all attempts were unsuccessful. This was largely due to the relatively low evaporation point of the Ru in the annealed rods, causing the quartz tube between the heating lamps and the material to fog up with RuO_2 powder,

and prevent significant heat transfer. This powder comes from the initial oxidation and sublimation of RuO_2 above 1000°C to more volatile states, before depositing on the cooler sides of the quartz tube and reducing back to RuO_2 [21]. This, combined with the high melting temperature of the material caused the 1500W lamps available to be insufficient for the melting step of optical floating zone crystal growth. In the future this could be potentially solved through employing a cooling trap at the top and bottom of the quartz tube, causing the RuO_2 powder to instead build up away from the lamps. Unfortunately, one was not available so no melting was achieved and no crystals could be produced at McMaster. The melting issue was overcome through use of 2000W Xenon arc-lamps at the University of Montreal. Two growths were attempted, but RuO_2 powder deposits resulted in difficult growing conditions. As such, only polycrystalline samples could be procured from these growths, as seen in Figure 5.1. These samples possess both crystalline and non-crystalline regions, and since it is unlikely that subjecting these samples would create a uniform electric field through the samples, these are inadequate for current-based μSR experiments.

As single crystals were necessary for the crystals used in the experiment were supplied to us by Dr. Braden's group at the University of Cologne. In total, 4 small $\sim 1\text{mm}^3$ -sized pure Ca_2RuO_4 crystals and 2 slightly larger $\sim 10\text{mm}^3$ -sized 1% Ti doped Ca_2RuO_4 crystals were received.

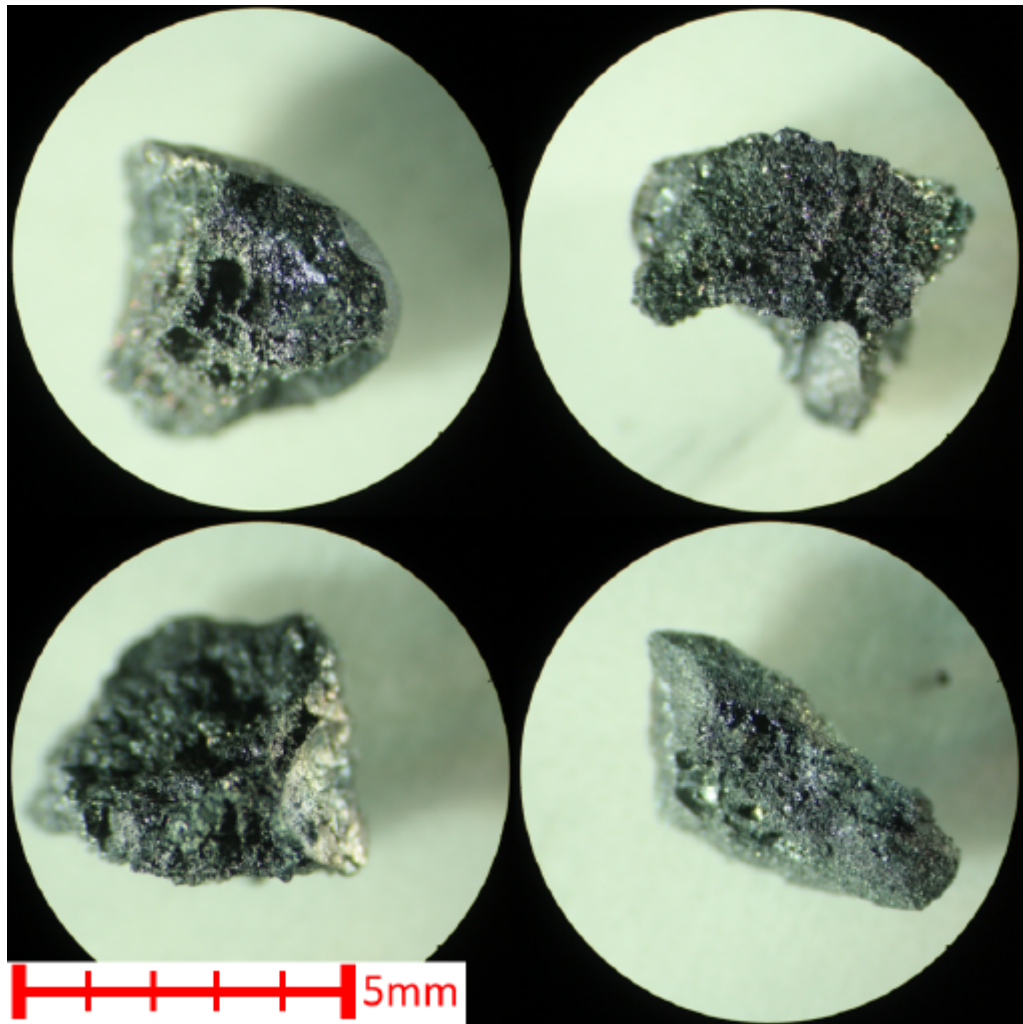


FIGURE 5.1: An image of pieces of a growth of 1% Ti doped Ca_2RuO_4 done at the University of Montreal. Some regions are reflective while others are not, indicating the presence of both crystal and powder regions. This is not adequate for an experiment with an applied current.

Chapter 6

μ SR Experiment at TRIUMF

6.1 μ SR and study goals

This project aims to investigate the magnetic phase transitions of a 1% Ti doped variety of the Mott insulator Ca_2RuO_4 using μ SR techniques. Using μ SR for this study allows us to probe the local magnetic fields in the crystal lattice. For this project, we pass a current through single crystal 1% Ti doped Ca_2RuO_4 while in the muon beam at TRIUMF to see the effects of different currents on the local internal magnetic fields. More specifically, we seek to determine whether the current induced Mott transition still exists in 1% Ti doped Ca_2RuO_4 and to investigate the magnetic properties of the metallic state. Both are accomplished through zero field temperature sweeps from ambient temperature to base temperature under select current values.

Previous μ SR experiments were performed and published by Carlo et al., who looked primarily at asymmetries of various dopings in the $\text{Ca}_{2-x}\text{Sr}_x\text{RuO}_4$ series in order to create a new magnetic phase diagram for the series [22]. Most relevant to our experiment, pure Ca_2RuO_4 measurements were performed and published in the supplementary information, as seen in Figure 6.1 [22]. We essentially seek to discover whether this behaviour is also appropriate for 1% Ti dopings, and whether current will eliminate the oscillations

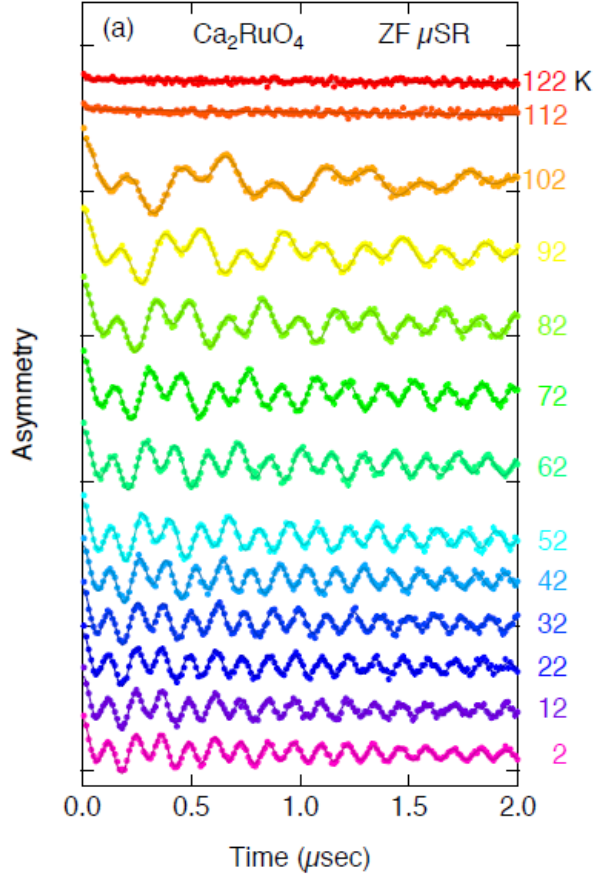


FIGURE 6.1: A waterfall plot of the temperature sweeps performed by Carlo et al. on pure Ca_2RuO_4 . This plot shows a clear ordering temperature between 112K and 102K, with two clearly defined muon spin frequencies seen below ordering temperature [22].

seen in the low temperature data which would suggest that current also eliminates the magnetic ordering seen in the sample.

6.2 μSR testing setup

6.2.1 The Sample Holder

Sample size was a great concern for the experiment, as too small a sample cannot give a strong signal in μSR . This is because the muon beam can be tuned to approximately 1

cm² in size, resulting in a poor signal to noise ratio if the sample was significantly smaller. Too large, however, and the heat generated by the sample can become increasingly notable, leading to increased doubts about what the helium bath thermometer says about the sample temperature. For this reason, the initial setup involved placing the two 1% Ti doped Ca₂RuO₄ pieces on an ultra thin silver backing and attaching wiring to each end to allow current to run through. The silver backing used was 13µm in thickness, which would provide stability and relatively little stopping power to the muon beam, allowing it to hit its intended target. In addition, silver is ideal as a backing metal as it produces a non-relaxing signal when seen in asymmetry plots due to the small nuclear dipole moment of silver and the absence of electronic magnetism, allowing simple background subtraction.

To prevent electrical conduction through the silver backing, Kapton tape was used to insulate the silver from the current-carrying wiring. Epoxy resin was used to attach the crystals to the Kapton tape, and thin silver wires were attached to the crystals with silver epoxy to allow current to run through the crystals. These wires formed a 2-point probe on the sample to the connectors that attach to the wiring of the sample rod. From the connectors through to the power supply, this transitioned to a 4-point probe to reduce the effect of the resistivity of the wiring on our measurements. Finally, for reasons explained later, the only sample used under current in this experiment was the larger of the two pieces, as seen in Figure 6.2, measuring approximately 0.84mm x 1.77mm x 6.50mm, which is still quite large compared to most pure Ca₂RuO₄ crystals.

6.2.2 Optimizing Signal to Noise

Given the thickness of the crystal, for best signal it was decided that the sample should be placed with the muon beam hitting the crystal before the silver backing. With a thinner crystal, a greater signal might be achieved through reversing this, as muons

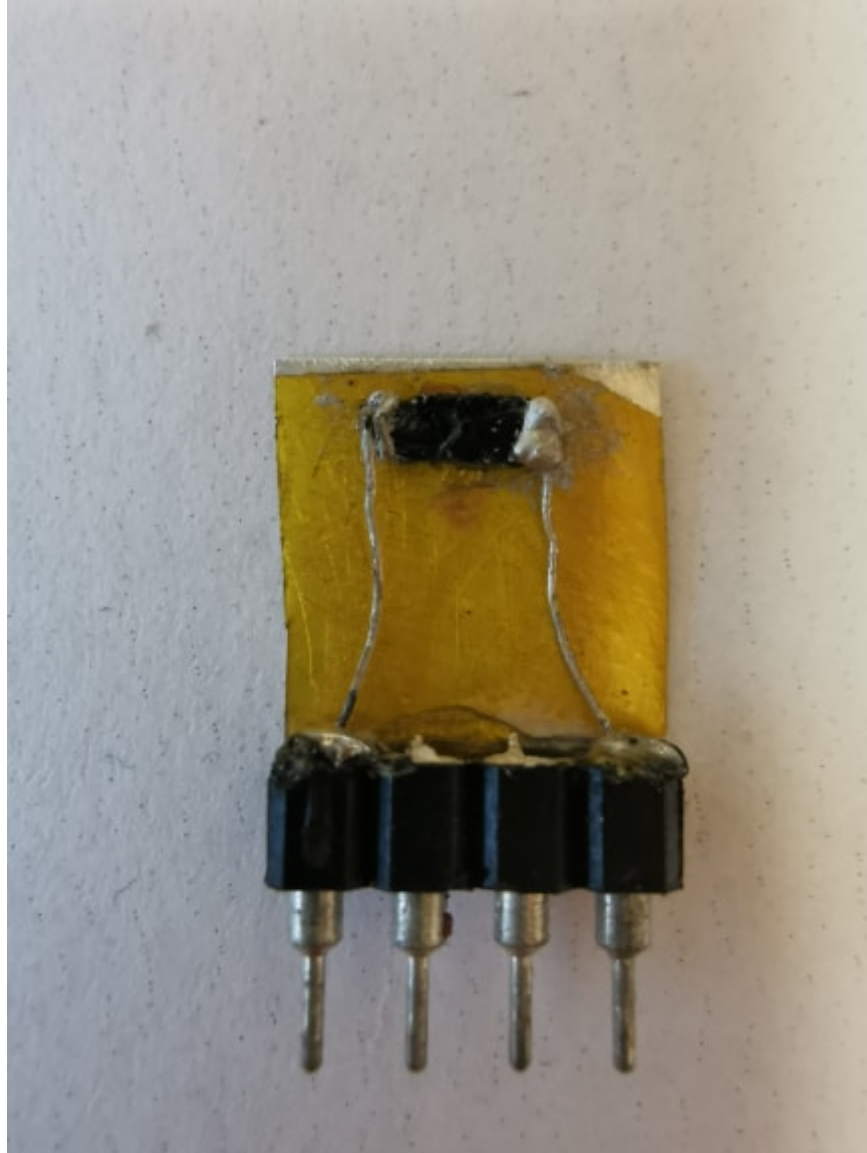


FIGURE 6.2: An image of the largest 1% Ti doped Ca_2RuO_4 sample before being attached to the sample rod. The two-point probe setup consists of silver wires and silver epoxy connecting the crystal to the connectors, which are then connected to the sample holder. From the sample holder to the power supply, the setup transitioned to a four-point probe to reduce the effects of the wiring on our measurements. This apparatus sits on a thin silver backing coated with Kapton tape.

need to travel a short distance through a solid before losing enough momentum to stop in the sample.

The muon beam was also tuned in an attempt to match the dimensions of the sample crystal as closely as possible. Tuning was performed by cutting out a hole in a thick piece of silver in the size, shape, and position of the 1% Ti doped Ca_2RuO_4 crystal tested. When placed in the beamline, shrinking and shifting the beam window allowed for the optimization of the ratio of muons that would avoid the silver altogether and would fail to be counted compared to the total muons in the beam. Muons that would miss the silver plate are the muons that are in position to hit the Ca_2RuO_4 sample when it is in the beamline, and thus the number of failed detections here should be maximized. This resulted in a signal to noise ratio of between 5–10% during the experiment, which could potentially still be improved, but was sufficient for an initial experiment under muons.

6.3 μSR Results

In the initial setup, the two large Ti doped single crystals were secured and wired on the ultra thin silver. This changed after the 0mA current run, however, as when the current was switched on it was discovered that the current was not flowing through the smaller of the pieces. Due to time constraints, instead of setting the crystal a second time and reapplying silver epoxy for the wire connections, we decided that it would be preferable to simply detach the smaller crystal. This would also simplify any electronic calculations done during the experiment.

6.3.1 Zero-Current Measurements

A zero-field temperature sweep performed in the absence of an external current can be seen in Figure 6.3. Initially, the higher temperature curves are typical exponential curves, showing a drop in asymmetry over time from a relaxation of the muon polarization away

from the back counter. Our sample can be seen to have an ordering temperature between 100K and 110K, which corresponds with previously reported ordering temperatures. That is because, below these temperatures, we can see well-defined oscillations in the asymmetry signal, revealing a narrow distribution of local magnetic fields at the muon site, consistent with long-range ordering. This also agrees with previously published μ SR data on pure Ca_2RuO_4 , which shows antiferromagnetic ordering below 110K and two local fields, which can be seen in 6.1 [22].

One oscillation frequency is clearly visible in our data, but a second could not be discerned, possibly due to the poor signal to noise ratio, and a higher relaxation rate than in pure Ca_2RuO_4 muon sites. Since the muon spin precession frequency is proportional to the static local field, a Fourier transform of the data can be used to reveal that there is a dominant local field at approximately 750G. This is equivalent to a muon spin precession frequency of $\nu = (13.554\text{MHz/kG})H = 10.84\text{MHz}$, notably higher than both frequencies in Carlo et al. [22]. This difference is present across sub-ordering temperatures that were looked at, as seen in 6.4. Both muon signals of unique frequencies seen in pure Ca_2RuO_4 are approximately equal in amplitude, so a lack of a second discernable field could be due to the poor signal to noise ratio in the experimental setup, a difference in the quantity and location of the muon sites due to the 1% Ti substitution, or a higher damping effect from the doped form being less homogeneous [22].

6.3.2 Applied Current Measurements

In the applied current runs performed, currents of 30mA and 100mA were selected based on resistivity data suggesting that 30mA would be just enough to produce a reported destruction of order and paramagnetic effect, while 100mA would give us a look well into this phase while still being a low enough current for our setup [20, 23]. As such, zero-field μ SR measurements were made for 1% Ti-doped Ca_2RuO_4 under 30mA and 100mA currents, as seen in 6.5 and 6.6, respectively. These waterfall plots demonstrate

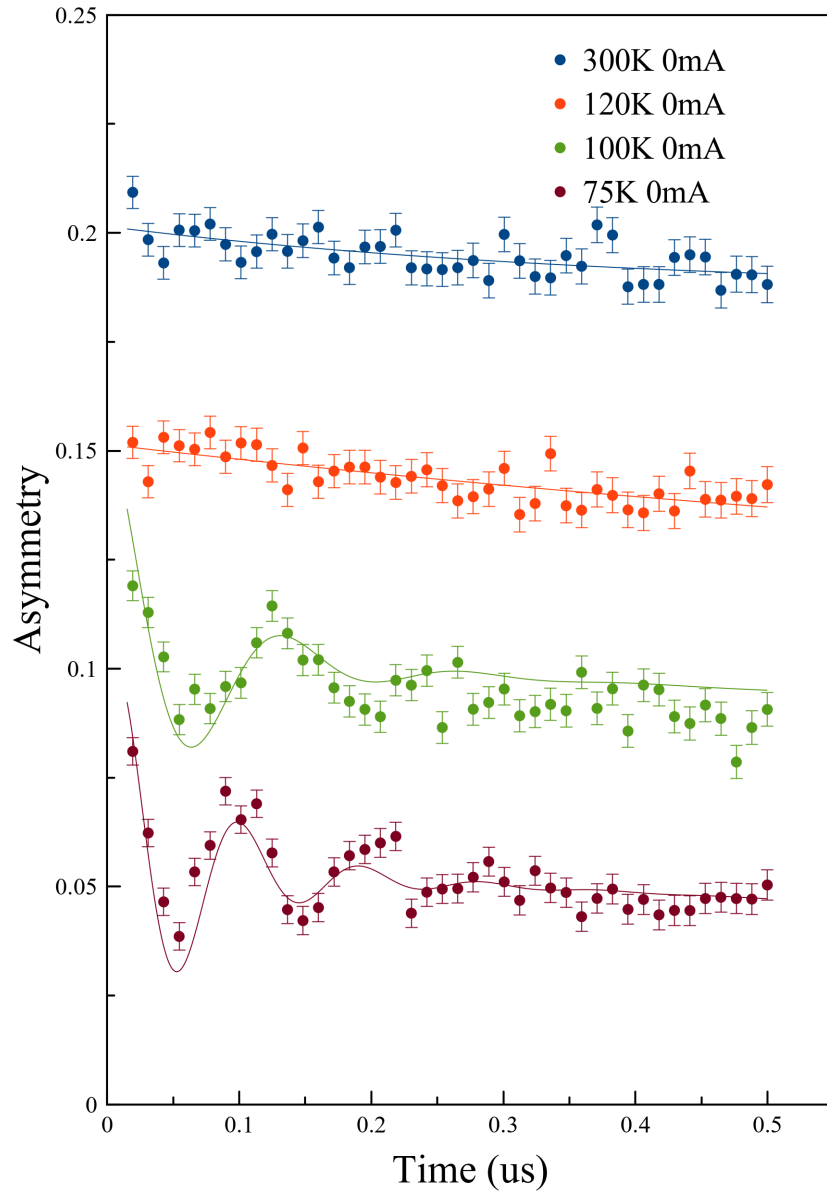


FIGURE 6.3: A temperature sweep in waterfall plot style for the 0mA runs under zero applied field. Waterfall runs are offset from each other by 0.05 asymmetry. There is a clear indication of magnetic ordering in the 100K and 75K runs, suggesting that antiferromagnetic ordering is present, as one would expect in a Mott insulator.

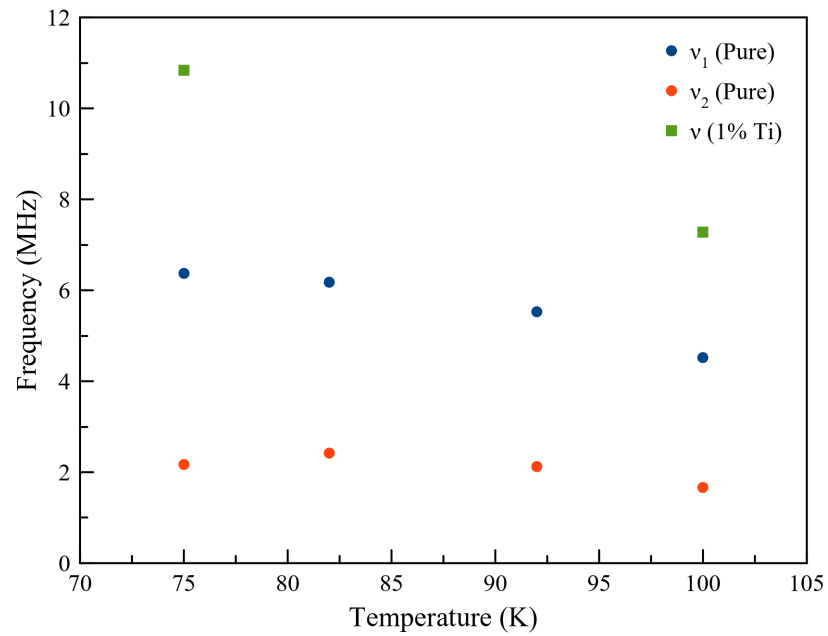


FIGURE 6.4: A plot of the muon spin frequencies seen in pure Ca_2RuO_4 from Carlo et al. and 1% Ti doped Ca_2RuO_4 taken in this thesis. The frequency seen in the Ti doped sample is higher than both pure sample frequencies.

a lack of strong magnetic ordering seen down to a nominal temperature of 50K for 30mA current, and 12.5K for 100mA current, seen in Table 6.1.

TABLE 6.1: A table relating applied current values to their equivalent current densities, as well as the lowest nominal temperature achieved using a 48V power supply. In the case of zero-current, the lowest temperature is the lowest that was deemed necessary to show long-range ordering.

I_{app} (mA)	J_{app} (A/cm ²)	Lowest Temperature (K)
0	0	75
30	2.0	50
100	6.7	12.5

It is important to emphasize that these are only nominal thermometry readings, which considering the presence of Joule heating, may not be a true representation of the sample temperature. If Joule heating is temporarily neglected, these results would confirm previously reported data that suggests that under a sufficient current, Ca₂RuO₄ will remain in a paramagnetic phase after its structural phase transition to the L-phase of the material [16]. This additionally agrees with early pressure studies into the material, which indicate that a paramagnetic phase occurs in the L-phase of the material above 0-25K, depending on the pressure applied, while below this a ferromagnetic regime can be found [11].

The temperature sweep of the 30mA current runs was cut short at 50K as at this point the resistance of the sample was high enough that our 48V power supply reached the voltage limit. Lower temperatures were achievable in the 100mA current runs due to the significantly decreased resistivity of the sample, but sub-14K temperatures could not be achieved in the He-4 cryostat.

6.4 Temperature control and Joule heating

Joule heating was a primary concern when attempting to accurately characterize Ca₂RuO₄ under current, as the accuracy of the thermometry used must be determined to ensure

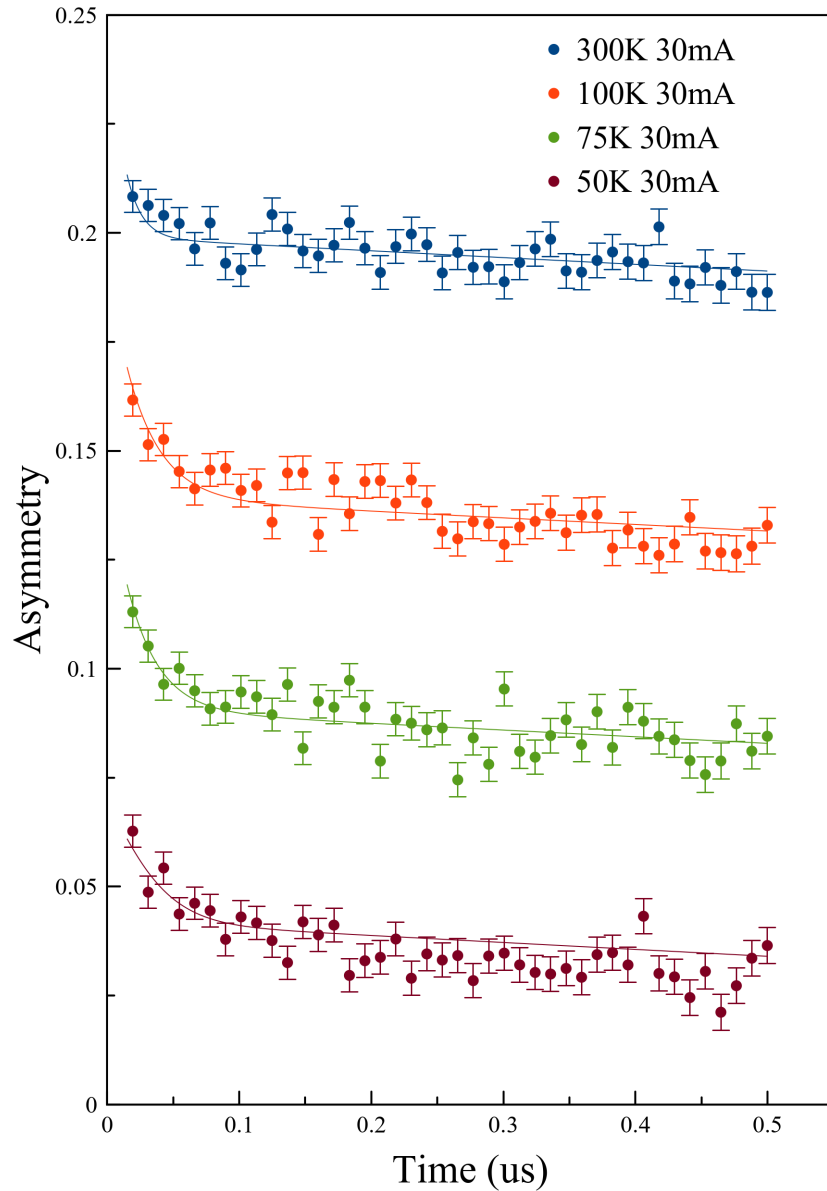


FIGURE 6.5: A temperature sweep in waterfall plot style for the 30mA runs under zero applied field. Waterfall runs are offset from each other by 0.05 asymmetry. There is no longer any strong indication of magnetic ordering down to 50K, suggesting that there was a phase transition out of the Mott insulating state.

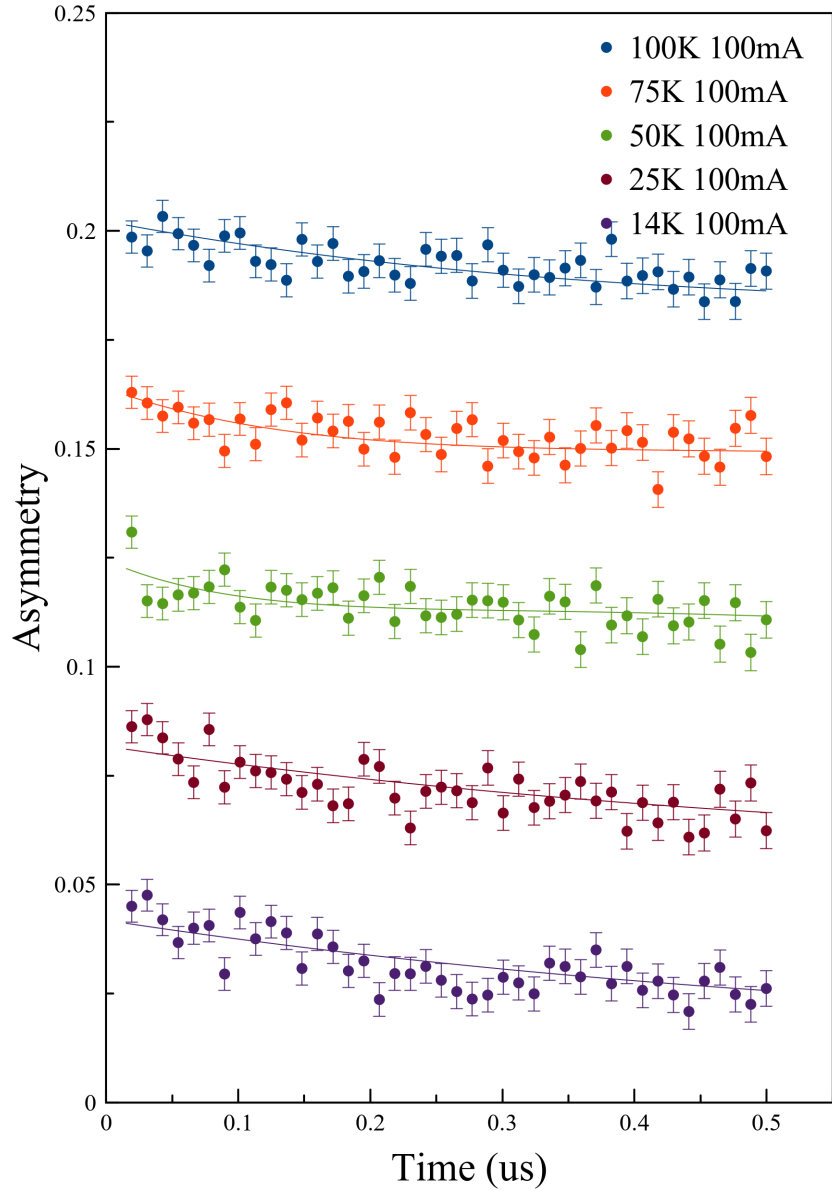


FIGURE 6.6: A temperature sweep in waterfall plot style for the 100mA runs under zero applied field. Waterfall runs are offset from each other by 0.04 asymmetry. This plot is very similar to the plot for 30mA, but confirms that ordering cannot be definitively seen to an even lower temperature of 12.5K. A lower temperature could be achieved due to the lower resistance causing a lower voltage, preventing our power supply from capping at 48V as in the 30mA runs.

sub-ordering temperatures were achieved. Thus, special care must be taken to ensure the recorded temperatures are close to the actual temperatures in the sample, and estimate how different these temperatures are.

In general, passing a current through a crystal with notable resistance will increase its temperature relative to its surroundings. Since our thermometer was not directly attached to the sample, we cannot know whether the temperature data in the applied current data above accurately describes the sample temperature, as we do not know how well the sample temperature is coupled to the environment. Previous works have shown that, in general, applying currents similar to what we have done here has been sufficiently cooled by a standard flowing He-4 cryostat similar to the one used by us while at TRIUMF [23]. As expressed in Fursich et al. in 2019, their paper on Raman scattering in Ca_2RuO_4 demonstrates through careful analysis of Stokes and anti-Stokes intensities that a current can prevent a Mott transition from occurring below the currentless ordering temperature without significant Joule heating [23]. Our own analysis seeks to determine whether this is valid for our testing apparatus specifically.

The sample thermometer used in our experiments was not directly on the sample, but was instead attached on the lower end of the sample holder in close proximity, a few centimeters away from the sample. This renders the temperature given by the thermometer to be primarily an approximation of the temperature of the cryostat's flowing helium bath rather than explicitly a sample temperature reading. Expanding on this point, power generation from the 1% Ti doped Ca_2RuO_4 sample used was calculated for all temperatures and currents, using the recorded current and voltages of each trial and $P = IV$. The sample was seen at lowest temperatures to provide a power output up to approximately $0.93W$, as seen in 6.7, which is a significant output for a small sample. This level of power output should cause significant Joule heating in the sample, which may not be sufficiently cooled by the helium bath. This would in turn mean that the

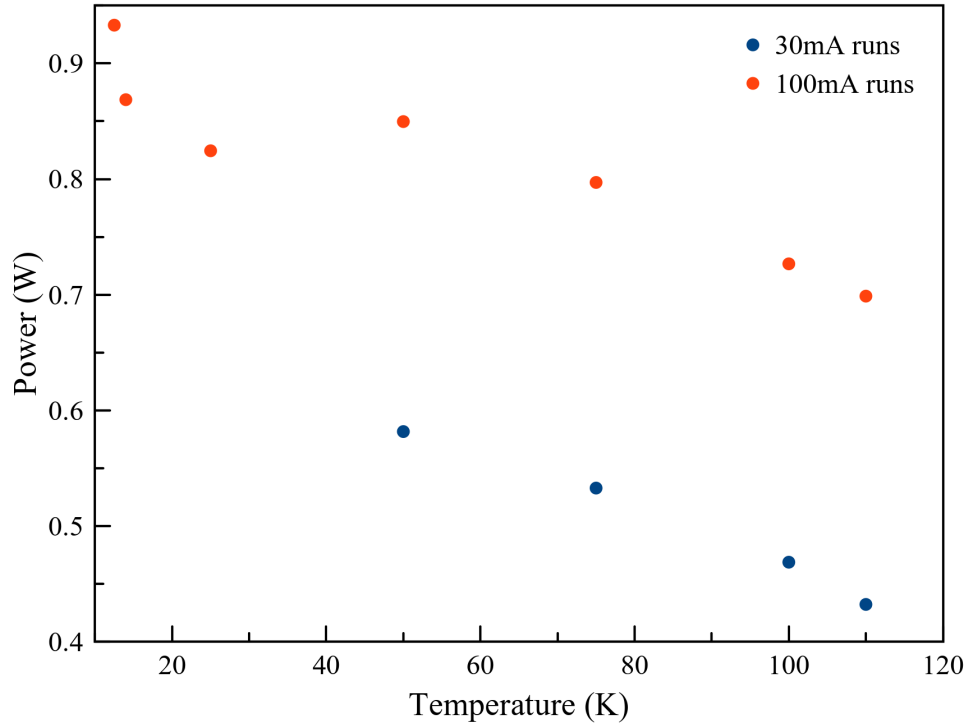


FIGURE 6.7: Approximate power generation of the 1% doped Ca_2RuO_4 sample at different thermometer readings. These values were calculated from collected resistance and voltage data during each run.

sample temperature is actually a higher temperature than the thermometer's nominal reading, and thus the thermometer itself cannot be solely relied on.

6.4.1 Convective Heat Transfer Calculations

It is difficult to determine the difference in recorded temperatures and sample temperatures, but some inferences can be made. Most notably, the lowest temperature achieved under current was 12.5K during 100mA current runs. This is in contrast to the normal lowest achievable temperature of the He-4 cryostat, which is about 2K. Without knowing the power dissipation capability of the helium cryostat, no strong indications of sample temperature can be directly claimed. However, the convection cooling power required

for sub-ordering temperatures can be analyzed to bring us closer to an answer, using the basic convective heat transfer equation,

$$\frac{Q}{A} = h(T - T_b) \quad (6.1)$$

where Q is the heat transferred per second, A is the surface area of the sample, h is the heat transfer coefficient in W/m^2K , T is the sample temperature, and T_b is the temperature of the flowing gaseous helium bath. In this calculation to determine whether the sample temperature is truly below an ordering temperature of 110K, we need to have a reasonable assessment of the heat transfer coefficient. Unfortunately, this is not so straightforward, as it is dependent on not just the helium flow rate, which is known to be approximately 1.2L/hr for this cryostat, but also properties such as the fluid density, specific heat capacity, kinematic viscosity, thermal conductivity for the specific pressure, temperature, and dimensions of the cryostat. Fortunately, we can estimate the lower bound of h with some assumptions.

We consider the 100mA temperature sweeps. In this sweep, the thermometer reading was stabilized at 14K for a run, then brought down to the lowest point achieved at 12.5K according to the nominal thermometer reading. Taking these temperatures to be T_b in respective runs, and the power generated by the sample in each run to be Q since this is the heat that must be removed from the sample to create a steady state, we can use a useful property of the power values to our advantage in finding h . We know that the power of the lower of the two temperature runs was higher despite constant current (0.93W compared to 0.87W), consistent with the expected relationship of resistivity increasing when temperature decreases. This means that the $T_{b2} = 12.5K$ run can be assumed to have a sample temperature lower than in the $T_{b1} = 14K$ in order to facilitate a higher resistivity in the sample. In other words, $T_2 < T_1$. So, first we isolate T , then

create an inequality from this relation and $T_2 < T_1$ to find our missing variable h 's lower bound.

$$\frac{Q}{A} = h(T - T_b) \quad (6.2)$$

$$T = \frac{Q}{Ah} + T_b \quad (6.3)$$

$$\frac{Q_1}{Ah} + T_{b1} > \frac{Q_2}{Ah} + T_{b2} \quad (6.4)$$

$$h > \frac{Q_2 - Q_1}{A(T_{b1} - T_{b2})} \quad (6.5)$$

Substituting in the sample surface area of $A = 3.69^{-5}m^2$, $Q_1 = 0.87W$, and $Q_2 = 0.93W$, we arrive at a heat transfer coefficient of $h > 1084W/(m^2K)$. Setting $h = 1084W/(m^2K)$ and assuming the heat transfer coefficient is the same for all temperature and current runs will give us an estimate for the sample thermometry, summarized in Table 6.2. The assumption of h being the same across all runs is not always a fair assumption, as only the 14K and 12.5K runs had the helium flow rate set to the maximum, but this is sufficient for our purposes of demonstrating sub-ordering temperatures. Since the bulk of these calculations suggest that the sample temperatures are below ordering temperature, this provides evidence that sub-ordering temperature was achieved in this experiment while under current. The calculated heat transfer coefficient is partially backed up through sources such as Liu et al., 2014, which looks at ambient temperature helium's heat transfer coefficient in different scenarios, typically achieving numbers between 10^2 or 10^3 [24]. This is however in a much higher pressure and with a different

setup geometry, both of which significantly affecting the coefficient value, and no exact parallel could be found in the literature.

TABLE 6.2: A table showing the conversion between the thermometer temperatures of runs stated in previous sections to an estimated sample temperature. Here the temperature readout from the thermometry is taken to be near bath temperature, and is thus labelled T_b . Values assuming the calculated h value are given, in addition to values assuming a coefficient of $h/2$ which, although theoretically impossible according to the calculations above, helps demonstrate the level of leniency on this calculation.

T_b (K)	T (30mA, h) (K)	T (30mA, $h/2$) (K)	T (100mA, h) (K)	T (100mA, $h/2$) (K)
110	121	132	127	145
100	112	123	118	136
75	88	102	95	115
50	65	79	71	92
25	-	-	46	66
14	-	-	36	58
12.5	-	-	36	59

6.4.2 Resistivity Anomalies

Placing the 1% Ti doped Ca_2RuO_4 sample in the μSR cryostat for dedicated resistance measurements and further looking through the initial data collected reveal some anomalies in the resistance data worth analysis. Our sample resistivity is an order of magnitude lower than reported for pure Ca_2RuO_4 , as seen in 6.8, but this is consistent with Kunke-moller et al., which demonstrates that a key difference in physical properties between pure and 1% Ti doped samples is nearly an order of magnitude difference in resistivity while in its conducting phase [20, 18]. This difference is unintuitive, as the addition of impurities would typically increase scattering and increase sample resistivity. This reduction in resistivity could be because the distortions to the lattice caused by the 1% Ti doping, reducing the tilting of the RuO_6 octahedra, might make the material less of a Mott insulator. Alternatively, this could be because the structural stability given by the doping could prevent any microscopic fissures that would increase resistivity and may be present in pure samples due to the more violent structural transition just above

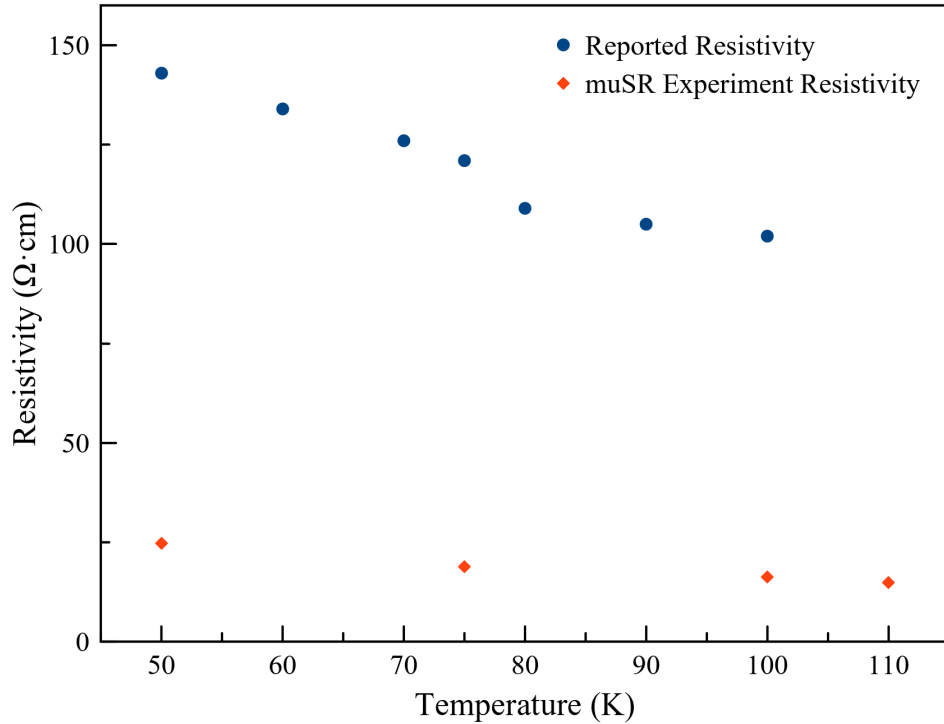


FIGURE 6.8: A comparison between the published resistivity of pure Ca_2RuO_4 with our collected 1% Ti doped resistivity data. Note that the difference is a factor of approximately 5 times.

room temperature. The resistivity collected in Kunkemoller et al. is only reported for temperatures above 300K, meaning there is currently no resistivity data to give a direct parallel. However, the ambient temperature data reported puts the resistivity of the 1% Ti doped crystal an order of magnitude lower than the pure sample, much like our data. One consequence of this is that the possession of a lower resistivity should lead to lower power dissipation compared to pure samples, so despite the comparatively large size of our sample, the power dissipation should be less than previous experiments on pure samples.

Another anomaly is that the resistivity data collected on our sample shows a drop in resistivity at a point below ordering temperature near 75K, which comes up in the

initial data collection as well, but occurs inconsistently, as seen in 6.9 and 6.10. This drop is only observed in some of the temperature sweeps, and the drop's appearance is independent of the applied current. This drop has been seen in some of the pure samples tested in Sow et al., consistently occurring between 70K and 90K [20]. This is also notably opposite of what has been seen to occur in Zhao et al., where it was seen that in “trained” and “untrained” samples had a jump up in resistivity near 80K, though it is worth noting that a 3% Mn substitution was used there instead of Ti for stability [16]. The reason for this difference is currently unexplained, but given that the temperatures of occurrence for both sources and the data collected here are similar, this suggests that our thermometer readings are similar in accuracy to the papers that published the present current-induced resistivity data on pure Ca_2RuO_4 . Since both papers had access to direct contact sample thermometry, this would suggest that our data collection is valid for our purposes, as it would indicate we achieved sub-ordering temperatures. Any analysis beyond the simple observation of destruction of order would be an exaggeration of the certainty of our temperature readings, however, as exact temperatures are still unknown.

6.4.3 Carbon Resistor Measurements

In order to further investigate the claim of whether sub-ordering temperatures were achieved with our own data, we performed resistance measurements on a 50Ω carbon film resistor in a lacquer coating under similar power conditions to the experiment in order to determine the temperature of the sample indirectly. A carbon resistor was used because its resistivity is less directly affected by current applied, and more affected by its present internal temperature, allowing us to look at resistivity of the resistor after calibration and make inferences about its temperature. The tests performed were first a near-zero current temperature sweep of the carbon resistor to calibrate it seen in 6.11, followed by a power sweep at 100K, 75K, 50K, and 25K, from minimal power generation to power

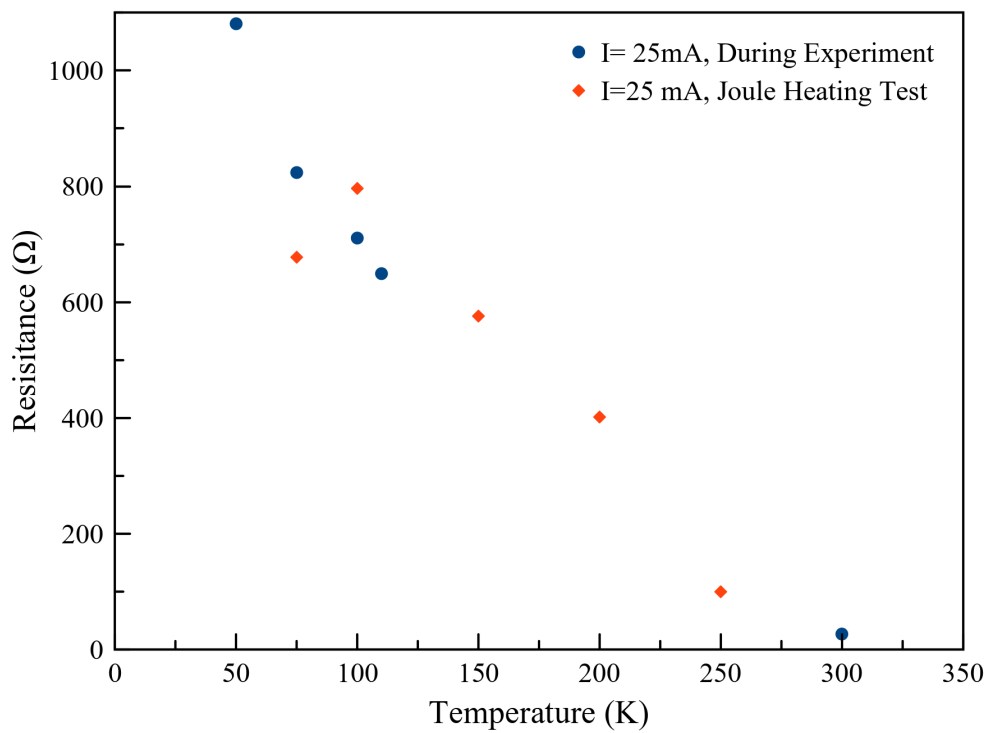


FIGURE 6.9: A comparison between resistance readings for 30mA runs during the experiment, and several months after. Note the large drop in resistivity between 100K and 75K, only occurring in a resistivity check performed months later which attempted to confirm our experiment resistivities.

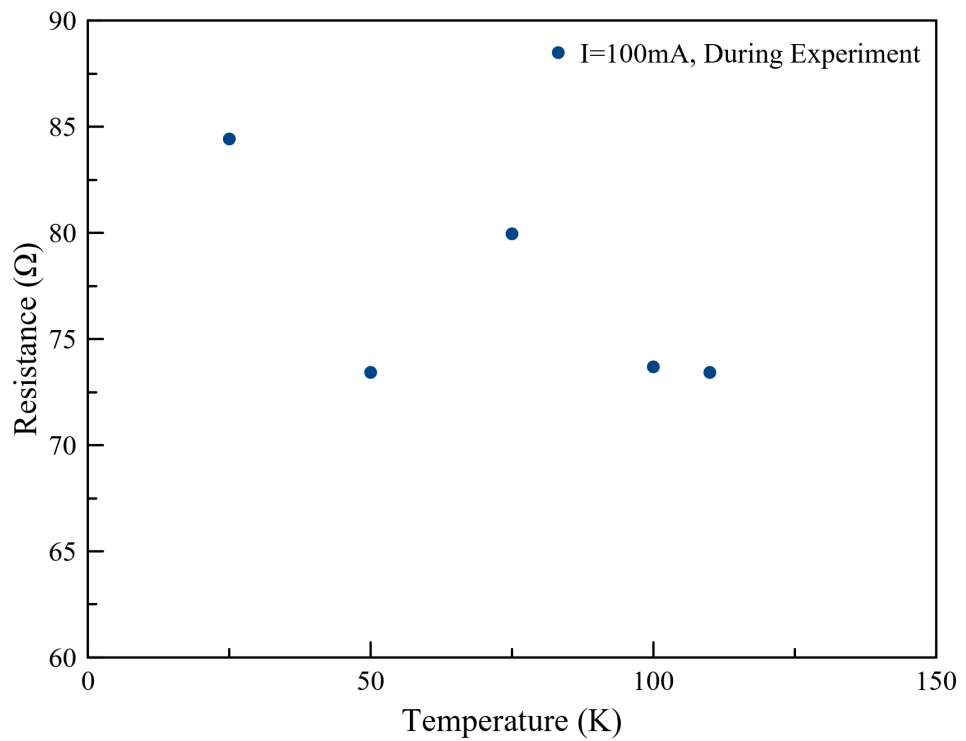


FIGURE 6.10: A temperature sweep for resistance readings on the 100mA runs during the experiment. Note the large drop in resistivity between 75K and 50K, demonstrating that this drop is inconsistent, and not purely a result of the separate resistivity checks performed later on.

above those achieved in Ca_2RuO_4 runs, seen in 6.12. From these, one can take power data from 6.7 to convert those into resistances that the carbon resistor would possess in each situation through 6.12 before finally being converted to a temperature from the calibration curve in 6.11. This process gives us data comparing nominal temperature readings to the “actual” temperature reading according to the carbon resistor calibration and sweeps, seen in 6.13. Worth noting is the fact that due to the sharp flattening of the curves for high power outputs in 6.12 and the fact that the highest power settings were not completed for the 50K nominal temperature reading, no extrapolations were made to plot the points in 6.13, meaning the 50K nominal temperature reading for the 100mA run was omitted from the plot.

The plot in 6.13 clearly suggests that sub-ordering temperatures were never achieved. This runs counter to all previous arguments, and certainly calls into question whether sub-ordering temperatures were achieved. There are, however, clear anomalies with this analysis. One of note is the 100K and 75K data points of the 100mA runs. These points are notably nearly identical, both possessing a 364K “actual” temperature. For similar reasons to those that justified the heat transfer coefficient analysis earlier, if both “actual” sample temperatures are the same, then there is nothing to account for the 10% increase in resistance between the two trials. This resistance discrepancy would need to be accounted for in some way other than a temperature change, and there is no such phenomenon seen in the current literature on the material. It is likely that the lacquer coating on the resistor thermally isolates the carbon resistor much more effectively than for the doped Ca_2RuO_4 sample. This would thus outline a “worst case scenario” for the nominal temperature readings, as an insulating coating could render the helium-4 bath ineffective at cooling the resistor.

From these anomalous points in the data, it is questionable how applicable the carbon resistor data is to our doped Ca_2RuO_4 experiment. The existence of this data, however,

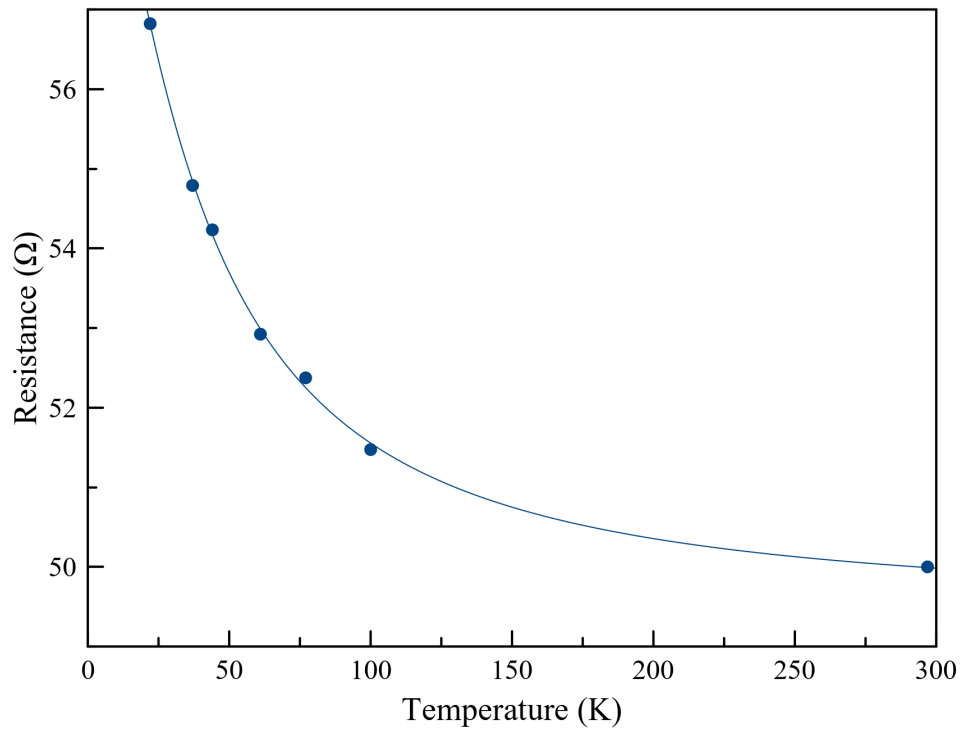


FIGURE 6.11: The measured calibration curve for the 50Ω carbon resistor used. This is used to translate the carbon resistor's resistance value while outputting a given power to the approximate temperature the resistor currently is to compare with the cryostat thermometer reading

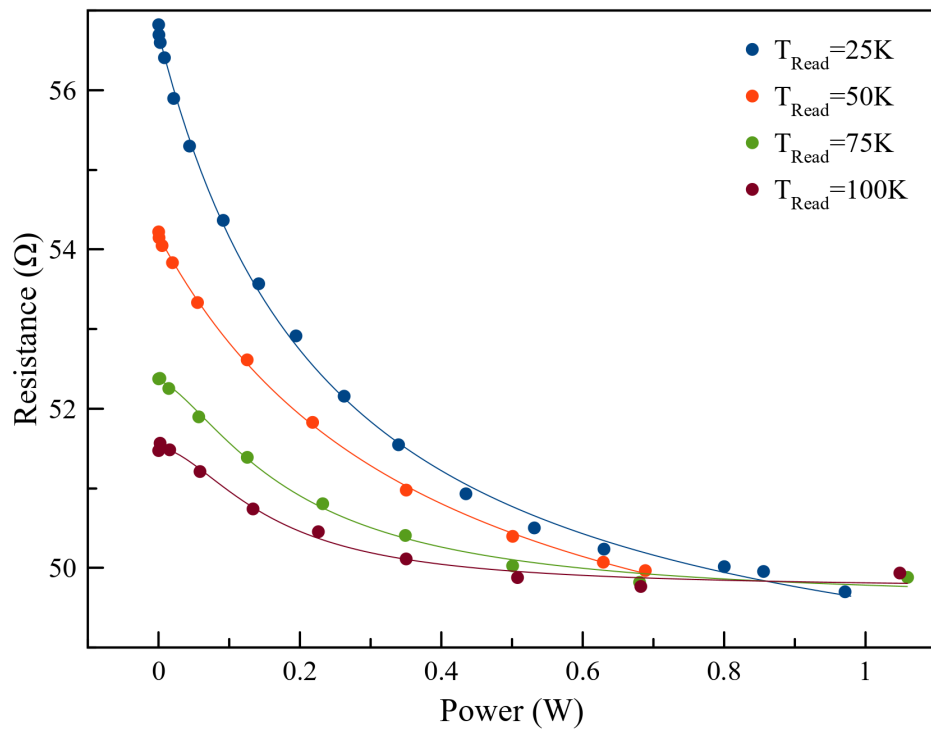


FIGURE 6.12: Power sweeps performed on the 50Ω carbon resistor in nominally isothermal conditions according to the thermometry. Power output was created with the same 48V power supply used for the Ca₂RuO₄ experiment, with measured power outputs of the crystal being within the power output curves here for each temperature.

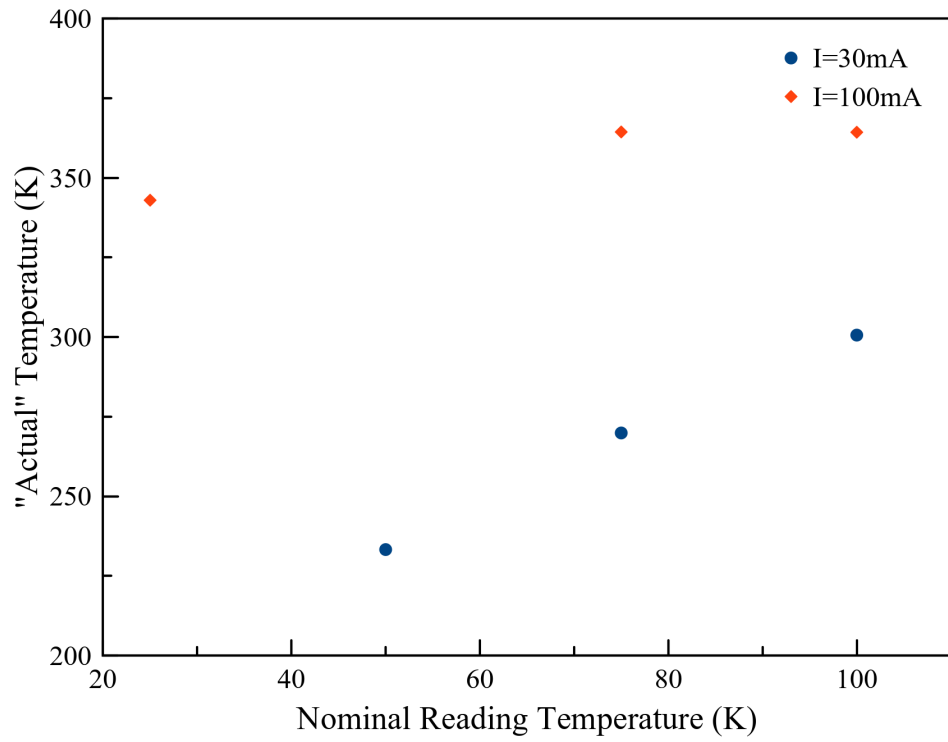


FIGURE 6.13: A plot of the nominal temperature readings during the Ca_2RuO_4 experiment compared to what the actual sample temperature was according to the carbon resistor analysis.

suggests extreme caution before validating these results without a better method of thermometry during Ca_2RuO_4 experiments in the same cryostat. This therefore leaves the question of whether sub-ordering temperatures were achieved not fully answered.

6.5 Summary

Our observations are naively consistent with those previously reported in Zhao et al., 2019 [16]. We see no long-range ordering upon application of current, and do observe long-range ordering below $T_N = 110\text{K}$ in the absence of an external current. This is despite greatly surpassing the transition boundary at $0.1\text{mA}/\text{cm}^2$, which translates to an applied current in our experiments as approximately 1.5mA . Data collection nearer to this boundary was not practical for our setup as the resistance of Ca_2RuO_4 under this current would cause our 48V power supply to reach its capacity well above ordering temperature. This is unfortunate, as investigations in low, yet non-zero current would be useful for confirming the boundaries of the phase diagram put forward in [16].

An indirect analysis of the thermometry of the setup used in our experiment shows that it is likely that sub-ordering temperatures were achieved as the nominal temperature readings would suggest. This is called into question through the carbon resistor analysis performed which contests this conclusion. The results are therefore inconclusive on whether sub-ordering temperatures were achieved, and more accurate temperature probing can be done in follow-up experiments to provide a more definitive explanation.

Chapter 7

Conclusions

7.1 Research Summary

This thesis sought to use μ SR techniques to analyze single crystal, 1% Ti doped Ca_2RuO_4 in order to investigate the electromagnetic properties of this material under a modest applied current. Pure as well as 1% Ti doped samples were synthesized, but no single crystals could be produced at McMaster University so the single crystal used in the experiment was sent by Dr. Braden's group at the University of Cologne. This gave a 1% Ti doped Ca_2RuO_4 crystal on the order of 1mm^3 in size.

Data collection at TRIUMF on the M20 beamline consisted of 3 temperature sweeps with a magnetic field of zero. These sweeps were a zero current temperature sweep, a 30mA temperature sweep, and a 100mA temperature sweep. The zero current sweep was taken below ordering temperature to confirm the presence of ordering below the published Neel temperature, while the applied current sweeps were taken to as low of a temperature as could be done with a 48V power supply. What was seen was the ordering in the zero current sweep was noticeably absent from the applied current runs, suggesting that the current successfully forced the Ca_2RuO_4 crystal into a different magnetic state in addition to a different structural state.

We then sought to investigate the validity of these results through analysis of the thermometry used. It could be seen that previous literature with stronger thermometry than our own possessed sub-ordering temperatures, and possessed notable resistance anomalies in their data at similar temperatures to our own nominal temperatures. These are largely speculation, however, so a more mathematical approach was taken to identify the minimum heat transfer coefficient of the cryostat, using that to determine the sample temperatures from nominal temperatures. Such analysis revealed a coefficient value of $h > 1084W/m^2$. Using this coefficient in convection cooling calculations puts the lowest achieved temperature while under current at 36K, well below the zero current Neel temperature around 110K.

Contradicting this, placing a calibrated carbon resistor under the same power and temperature conditions suggest a significant Joule heating in the sample, one that would place it above ambient temperature in all 100mA runs performed. This leads us to be cautious about whether current suppresses the antiferromagnetic ordering transition.

7.2 Further Research

A followup experiment for Ca_2RuO_4 was approved at TRIUMF, with a proposal to improve the poor signal to noise ratio of the data and the reliability of the thermometry through use of a different apparatus. In addition, the followup would better characterize the destruction of magnetic ordering by testing more current values, allowing us to see where the transition takes place. Transverse field μ SR would also be used for Knight shift measurements to reaffirm that a diamagnetic response in Sow et al. 2017 was not a signal from Ca_2RuO_4 and was likely an artifact from their SQUID magnetometer. Unfortunately, the experiment was delayed due to TRIUMF's temporary shutdown due to COVID-19, and as such this data could not find its way into the present thesis.

Additional care for the followup experiment must be taken in regards to sample thermometry. A contact temperature probe is the most practical solution for improving thermometer accuracy, as this would reduce the discrepancy between the sample environment and the thermometer environment to a vanishing difference. Additionally, the experiment should be performed under a comparatively low current and higher voltage if a high voltage power supply is available, as this will reduce sample heating.

7.3 Conclusion

In conclusion, Mott insulator 1% doped Ca_2RuO_4 was found to undergo a structural phase transition under modest current densities, drastically lowering its resistivity to that of a conductor. The applied current μSR research presented shows no magnetic ordering below the currentless ordering temperature by the nominal temperature readings, but it is uncertain whether this is a result of the structural phase transition or current-induced Joule heating of the sample. Methods of determining the sample temperature under current in the cryostat proved inconclusive, with indirect evidence suggesting T_N temperatures were achieved, but other indirect evidence suggesting the opposite was true. More experimentation should be done in the future to investigate the magnetic nature of this state and confirm the accuracy of the thermometry analyses done here.

Bibliography

- MacKenzie, A. P. and Maeno, Y. (May 2003). The superconductivity of Sr_2RuO_4 and the physics of spin-triplet pairing. *Rev. Mod. Phys.* 75 (2), 657–712.
- Ishida, K., Mukuda, H., Kitaoka, Y., Asayama, K., Mao, Z. Q., Mori, Y., and Maeno, Y. (Dec. 1998). Spin-triplet superconductivity in Sr_2RuO_4 identified by ^{17}O Knight shift. *Nature* 396(6712), 658–660.
- Duffy, J. A., Hayden, S. M., Maeno, Y., Mao, Z., Kulda, J., and McIntyre, G. J. (Dec. 2000). Polarized-Neutron Scattering Study of the Cooper-Pair Moment in Sr_2RuO_4 . *Phys. Rev. Lett.* 85 (25), 5412–5415.
- Luke, G. M., Fudamoto, Y., Kojima, K. M., Larkin, M. I., Merrin, J., Nachumi, B., Uemura, Y. J., Maeno, Y., Mao, Z. Q., Mori, Y., Nakamura, H., and Sigrist, M. (1998). Time-reversal symmetry-breaking superconductivity in Sr_2RuO_4 . *Nature* 394(6693), 558–561. ISSN: 00280836.
- Luke, G., Fudamoto, Y., Kojima, K., Larkin, M., Nachumi, B., Uemura, Y., Sonier, J., Maeno, Y., Mao, Z., Mori, Y., and Agterberg, D. (2000). Unconventional superconductivity in Sr_2RuO_4 . *Physica B: Condensed Matter* 289-290, 373–376. ISSN: 0921-4526.
- Drude, P. (Feb. 1900). Zur Elektronentheorie der Metalle. *Ann. Phys.* 306, 566–613.
- Roy, S. B. (2019). *Mott Insulators*. IOP.
- Nakatsuji, S., Ikeda, S.-i., and Maeno, Y. (July 1997). Ca_2RuO_4 : New Mott Insulators of Layered Ruthenate. *Journal of the Physical Society of Japan* 66(7), 1868–1871. ISSN: 0031-9015.

Bibliography

- Friedt, O., Braden, M., André, G., Adelman, P., Nakatsuji, S., and Maeno, Y. (2001). Structural and magnetic aspects of the metal-insulator transition in $\text{Ca}_{2-x}\text{Sr}_x\text{RuO}_4$. *Physical Review B - Condensed Matter and Materials Physics* 63(17), 1744321–17443210. ISSN: 01631829.
- Braden, M. and André, G. (1998). Crystal and magnetic structure of Magnetoelastic coupling and the metal-insulator transition. *Physical Review B - Condensed Matter and Materials Physics* 58(2), 847–861. ISSN: 1550235X.
- Steffens, P., Friedt, O., Alireza, P., Marshall, W. G., Schmidt, W., Nakamura, F., Nakatsuji, S., Maeno, Y., Lengsdorf, R., Abd-Elmeguid, M. M., and Braden, M. (2005). High-pressure diffraction studies on Ca_2RuO_4 . *Physical Review B - Condensed Matter and Materials Physics* 72(9), 1–7. ISSN: 10980121.
- Nakamura, F., Sakaki, M., Yamanaka, Y., Tamaru, S., Suzuki, T., and Maeno, Y. (2013). Electric-field-induced metal maintained by current of the Mott insulator Ca_2RuO_4 . *Scientific Reports* 3. ISSN: 20452322.
- Cao, G., McCall, S., Shepard, M., Crow, J. E., and Guertin, R. P. (Aug. 1997). Magnetic and transport properties of single-crystal Ca_2RuO_4 : Relationship to superconducting Sr_2RuO_4 . *Phys. Rev. B* 56 (6), R2916–R2919.
- Cox, P. (1992). *Transition Metal Oxides*. Oxford.
- Okazaki, R., Nishina, Y., Yasui, Y., Nakamura, F., Suzuki, T., and Terasaki, I. (2013). Current-induced gap suppression in the mott insulator Ca_2RuO_4 . *Journal of the Physical Society of Japan* 82(10), 1–5. ISSN: 00319015.
- Zhao, H., Hu, B., Ye, F., Hoffman, C., Kimchi, I., and Cao, G. (2019). Nonequilibrium Orbital Transitions via Applied Electrical Current in Calcium Ruthenate. *Physical Review B* 100(24).
- Mizokawa, T., Tjeng, L. H., Sawatzky, G. A., Ghiringhelli, G., Tjernberg, O., Brookes, N. B., Fukazawa, H., Nakatsuji, S., and Maeno, Y. (2001). Spin-orbit coupling in

Bibliography

- the mott insulator Ca₂RuO₄. *Physical Review Letters* 87(7), 77202–1–77202–4. ISSN: 10797114.
- Kunkemöller, S., Komleva, E., Streltsov, S. V., Hoffmann, S., Khomskii, D. I., Steffens, P., Sidis, Y., Schmalzl, K., and Braden, M. (2017). Magnon dispersion in Ca₂Ru_{1-x}Ti_xO₄: Impact of spin-orbit coupling and oxygen moments. *Physical Review B* 95(21), 1–14. ISSN: 24699969.
- Fobes, D., Vehstedt, E., Peng, J., Wang, G. C., Liu, T. J., and Mao, Z. Q. (2012). Metal-insulator transition in doped Ca₂RuO₄: Potential application in bolometric detection. *Journal of Applied Physics* 111(8), 2–6. ISSN: 00218979.
- Sow, C., Yonezawa, S., Kitamura, S., Oka, T., Kuroki, K., Nakamura, F., and Maeno, Y. (2017). Current-induced strong diamagnetism in the Mott insulator Ca₂RuO₄. *Science* 1087(November), 1084–1087.
- Garisto, F. (1988). Thermodynamic behaviour of ruthenium at high temperatures. *AECL-9552*.
- Carlo, J. P., Goko, T., Gat-Malureanu, I. M., Russo, P. L., Savici, A. T., Aczel, A. A., MacDougall, G. J., Rodriguez, J. A., Williams, T. J., Luke, G. M., Wiebe, C. R., Yoshida, Y., Nakatsuji, S., Maeno, Y., Taniguchi, T., and Uemura, Y. J. (2012). New magnetic phase diagram of (Sr,Ca)₂RuO₄. *Nature Materials* 11(4), 323–328. ISSN: 14764660.
- Fürsich, K., Bertinshaw, J., Butler, P., Krautloher, M., Minola, M., and Keimer, B. (2019). Raman scattering from current-stabilized nonequilibrium phases in Ca₂RuO₄. *Physical Review B* 100(8), 1–6. ISSN: 24699969.
- Liu, Q., Zhao, Z., and Fukuda, K. (2014). Transient heat transfer for forced flow of helium gas along a horizontal plate with different widths. *International Journal of Heat and Mass Transfer* 75, 433–441. ISSN: 0017-9310.